Monthly Notices of the ROYAL ASTRONOMICAL SOCIETY

MNRAS **549,** 1–25 (2026)
Advance Access publication 2026 January 27

https://doi.org/10.1093/mnras/stag183

The K-dwarfs survey – I. Four validated planets from the radius valley to the Neptune desert

G. Morello [1,2★] A. Peláez-Torres [1] F. J. Pozuelos [1] M. Dévora-Pajares [3,4] F. Murgas [5,6] J. P. de Leon [7] B. Rojas-Ayala [8] A. Bieryla [9] K. Barkaoui [5,10,11] S. Yalçınkaya [12,13] Ö. Baştürk [12,13] B. V. Rackham [11,14] A. Burgasser [15] E. Pallé [5,6] N. Narita [5,7,16] R. Varas [1] P. J. Amado [1] N. Abreu García [5,6] I. Bonilla-Mariana,[6] Y. Calatayud-Borras [17] E. Esparza-Borges [5,6] G. Fernández-Rodríguez [5,6] I. Fukuda [18] A. Fukui [5,7] A. García-Serra,[5,6] S. Geraldía-González [5,6] J. González-Rodríguez,[5,6] Y. Hayashi [18] K. Ikuta [19] K. Isogai [18,20] Y. Kawai [18] K. Kawauchi [21] P. Klagyivik [22] J. Korth [23] G. Lacedelli [5,6] F. Libotte [5,24] J. H. Livingston [16,25,26] P. Montañés-Rodríguez [5,6] M. Mori [16,25] J. Orell-Miquel [27] H. Parviainen [5,6] M. Sánchez-Benavente [5] N. Watanabe [18] K. A. Collins,[9] R. P. Schwarz [9] C. Stockdale [28] F. P. Wilkin [29] R. Zambelli [30] M. E. Everett [31] D. R. Ciardi [32] C. A. Clark [32] M. B. Lund [32] M. Timmermans,[10,33] E. Ducrot,[34] M. J. Hooton,[35] P. P. Pedersen [35,36] A. Burdanov,[11] A. H. M. J. Triaud [33] J. de Wit,[11] F. Grau Horta [37] G. Domènech-Rams [38] E. Herrero [38] J. Lopesino [39] B. O. Demory [40] M. Gillon [10] Y. Gómez Maqueo Chew [41] A. Khandelwal,[41] M. Lendl [42] M. Pichardo Marcano [41] I. Plauchu-Frayn [43] D. Queloz,[35] U. Schroffenegger [40] F. Zong Lang,[40] J. F. Kielkopf [44] H. P. Osborn [40,45] A. Krenn,[46] Y. Alibert,[40,47] T. Wilson,[48] A. Deline,[23] A. Fortier,[40,47] P. F. L. Maxted [49] and M. N. Günther [50]

Affiliations are listed at the end of the paper

Accepted 2026 January 17. Received 2026 January 14; in original form 2025 October 17

ABSTRACT

Sub-Neptune-sized exoplanets are the most common class discovered by transit surveys, yet their detailed exploration has just begun. Their demographics have inspired models of planetary formation and evolution, though the sample is naturally biased toward the predominance of M-dwarf systems, which provide more favourable observing conditions. We aim to validate the planetary nature of four candidates identified by the *Transiting Exoplanet Survey Satellite* (*TESS*) orbiting K-dwarf stars: TOI-2133.01, TOI-5734.01, TOI-5938.01, and TOI-7009.01. We used photometric, spectroscopic, and high-resolution imaging data from the *TESS* Follow-up Observing Programme with well-established and cutting-edge tools for validating the planetary nature of the candidates. We validate all four candidates and determine their system parameters. TOI-2133 b and TOI-5734 b lie near the upper edge of the radius valley, while TOI-5938 b and TOI-7009 b are at the boundary of the Neptune desert, making them rare additions to the known sub-Neptune population. The planets are suitable for precise mass measurements and atmospheric characterization with current facilities, making them benchmark targets for testing formation and evolution models around K-dwarf hosts, a population less accessible than the typical M-dwarf systems.

Key words: methods: observational – techniques: high angular resolution – techniques: photometric – techniques: spectroscopic – planets and satellites: detection – planets and satellites: fundamental parameters.

1 INTRODUCTION

Sub-Neptunes, here referred to as planets with radii between that of Earth and Neptune (∼1–4 $R_\oplus$), are the most ubiquitous planets in the Milky Way, according to recent demographic studies (D. C. Hsu et al. 2019; M. Kunimoto & J. M. Matthews 2020; M. Kunimoto & S. Bryson 2021). Their lack of Solar system counterparts and the inherent compositional degeneracy make them both intriguing and challenging targets for study. The statistical distribution of planetary sizes reveals a deficit at ∼1.5–2 $R_\oplus$, known as the radius valley, suggestive of a dichotomy between super-Earths

★ E-mail: gmorello@iaa.csic.es

© The Author(s) 2026.
Published by Oxford University Press on behalf of Royal Astronomical Society. This is an Open Access article distributed under the terms of the Creative Commons Attribution License (https://creativecommons.org/licenses/by/4.0/), which permits unrestricted reuse, distribution, and reproduction in any medium, provided the original work is properly cited.

Downloaded from academic.oup.com/mnras/article/549/3/stag183/8442244 by UNIV LEIGE FAC PSYCH SCIENCES L'EDUCATION user on 26 November 2026

and mini-Neptunes (B. J. Fulton et al. 2017; B. J. Fulton & E. A. Petigura 2018). Density measurements further suggest a possible trichotomy among sub-Neptunes, including dry and water-rich rocky planets, and gas dwarfs with substantial H_2–He envelopes (R. Luque & E. Pallé 2022). Another prominent feature in the exoplanet population is the Neptune desert, a relative paucity of short-period planets with radii $\gtrsim 3\,R_\oplus$ (T. Mazeh, T. Holczer & S. Faigler 2016; A. Castro-González et al. 2024).

Several mechanisms have been proposed to explain these features in the observed exoplanet population. Atmospheric escape processes are thought to shape the statistical distributions of planetary radii and orbital periods, via photoevaporation (J. E. Owen & Y. Wu 2013, 2017) or core-powered mass loss (S. Ginzburg, H. E. Schlichting & R. Sari 2018; A. Gupta & H. E. Schlichting 2019, 2020). Formation loci and migration paths within the protoplanetary disk largely determine bulk elemental compositions, with the ice line separating dry from water-rich planets (E. Chiang & G. Laughlin 2013; B. Bitsch, S. N. Raymond & A. Izidoro 2019; A. Cevallos Soto et al. 2022). The mode of accretion, whether dominated by pebbles or planetesimals, further affects the efficiency of volatile delivery and enrichment (S. Chatterjee & J. C. Tan 2014; A. Izidoro et al. 2021a; A. Izidoro, B. Bitsch & R. Dasgupta 2021b). Alternative or combined formation and evolutionary processes have been invoked to explain the observed trends and diversity among sub-Neptunes. These include giant impacts (N. K. Inamdar & H. E. Schlichting 2015), magnetospheric rebound (B. Liu, C. W. Ormel & D. N. C. Lin 2017), high-eccentricity migration (J. E. Owen & D. Lai 2018), dissolution of H_2 in magma oceans (E. S. Kite et al. 2019), and protoplanetary disk dispersal (M. Ogihara, M. Kunitomo & Y. Hori 2020).

Discriminating among the many proposed formation and evolutionary pathways requires enlarging the sample of well-characterized sub-Neptunes. While many competing theories can reproduce the overall statistical distributions, they often predict different correlations with system parameters, such as orbital period, stellar insolation, mass and age (V. Van Eylen et al. 2018; T. A. Berger et al. 2020; J. G. Rogers et al. 2021; D. Jordan & I. Song 2025). These trends can be tested with a broad and finely sampled coverage of parameter space. Targets suitable for atmospheric characterization are particularly valuable, as they may help break compositional degeneracies, allowing more rigorous tests of formation and evolution models (A. Cevallos Soto et al. 2022; K. Heng, J. E. Owen & M. Tian 2025).

Most known sub-Neptunes orbit M dwarfs, whose small sizes and masses make them the easiest targets for transit and radial velocity observations. Planets around K dwarfs represent the next most accessible population, with the added advantage of being less affected by stellar activity, reducing the need for complex detrending (B. V. Rackham, D. Apai & M. S. Giampapa 2018, 2019; A. Biagini et al. 2024). Furthermore, K dwarf planets experience lower levels of XUV irradiation throughout their evolution, favouring the retention of primordial atmospheres and potentially more favourable conditions for the emergence of life (J. Lillo-Box et al. 2022).

In this work, we validate the planetary nature of four candidates identified by the *Transiting Exoplanet Survey Satellite* (*TESS*; G. R. Ricker et al. 2015) using three complementary approaches, spanning classical and cutting-edge methods: multi-colour photometry (H. Parviainen et al. 2019), statistical validation (S. Giacalone et al. 2022), and a novel neural-network classifier (M. Dévora-Pajares et al. 2025). TOI-2133.01, TOI-5734.01, TOI-5938.01, and TOI-7009.01 are likely sub-Neptunes orbiting K-dwarf stars. This paper is structured as follows. Section 2 presents the observations, including transit photometry, stellar spectroscopy, and high-resolution imaging. Section 3 describes the characterization of the host stars. Section 4 explains the three validation methods adopted in this work and the estimation of the final system parameters. Section 5 reports their outcomes. Section 6 discusses the scientific interest of these systems and prospects for further characterization. Section 7 summarizes our findings and motivates the continuation of the K-dwarf survey programme presented in this work.

2 OBSERVATIONS

2.1 *TESS* photometry

The four targets analysed in this work were identified as *TESS* Objects of Interest (TOIs) by the Science Processing Operations Center (SPOC) pipeline at NASA Ames Research Center (J. M. Jenkins et al. 2016). We retrieved the Presearch Data Conditioning Simple Aperture Photometry (PDCSAP) light-curves from the Mikulski Archive for Space Telescopes[1] (MAST). The PDCSAP flux is obtained through the SAP module (R. L. Morris et al. 2020) and corrected for crowding and instrumental systematic effects via the PDC module (J. C. Smith et al. 2012; M. C. Stumpe et al. 2014).

We used the 2-min cadence SPOC PDCSAP light-curves whenever available, as they provide the highest photometric quality and minimize smearing of the astrophysical signal due to finite integration time (D. M. Kipping 2010; G. Morello, A. Dyrek & Q. Changeat 2022). Only for TOI-7009 did we also use the High-Level Science Product Quick-Look Pipeline (QLP) 200-s light-curves (C. X. Huang et al. 2020), whose large number compensated for the availability of SPOC light-curves from just one sector. The *TESS* sectors analysed for each target are listed in Table 1. Figs 1 and B1 show the target pixel files (TPFs) and aperture masks used to extract the SAP flux, created using `tpfplotter` [2] (A. Aller et al. 2020). All targets have at least one fainter contaminant within the adopted *TESS* aperture (with $2 < \Delta m < 6$), except for TOI-7009, whose aperture includes a brighter neighbouring star. The flux contributions from contaminating sources are estimated and corrected by the PDC module, while QLP/HSLP light-curves include only partial deblending through their aperture-extraction process.

2.2 Follow-up photometry

The *TESS* pixel scale is 21 arcsec pixel^{-1} and photometric apertures typically extend out to roughly 1 arcmin, generally causing multiple stars to blend in the *TESS* photometric aperture. To determine the true source of the *TESS* detection, we acquired time-series photometry of the fields around TOI-2133, TOI-5734, TOI-5938, and TOI-7009 as part of the *TESS* Follow-up Observing Programme (TFOP; K. Collins 2019).[3]

2.2.1 *MuSCAT2*

MuSCAT2 is a four-colour simultaneous imaging camera mounted on the 1.52m Telescopio Carlos Sánchez (TCS) at the

[1] https://mast.stsci.edu
[2] https://github.com/jlillo/tpfplotter
[3] https://tess.mit.edu/followup

Downloaded from academic.oup.com/mnras/article/549/3/stag183/8442244 by UNIV LEIGE FAC PSYCH SCIENCES L'EDUCATION user on 26 November 2026

Table 1. List of transit observations, their main characteristics and auxiliary parameters used for detrending.

TOI ID	Instrument	*TESS* sector/ UT date	Passband	Exposure time (*s*)	Photometric aperture (″)	Detrending parameters
2133.01	*TESS*	25, 26, 52, 53, 79	*TESS*	120	>21	GP: Matérn-3/2 + Jitter
2133.01	MuSCAT2	2025 May 30	g', r', i', z_s'	10, 7, 4, 5	4.35	AIRMASS
2133.01	LCO-SAAO−1m0	2025 May 07	i'	26	5.6	Sky/Pixel_T1, Y(FITS)_T1
5734.01	*TESS*	20, 47, 60	*TESS*	120	>21	GP: Matérn-3/2 + Jitter
5734.01	MuSCAT2	2025 Mar 18	g', r', i', z_s'	8, 7, 5, 8	10.875	AIRMASS
5734.01	LCO-TEID−1m0	2023 Dec 11	z_s'	20	12.0	AIRMASS, X(FITS)_T1
5734.01	CHEOPS	2023 Feb 23	CHEOPS	54	15.0	Pipeline
5938.01	*TESS*	81, 82	*TESS*	120	>21	GP: Matérn-3/2 + Jitter
5938.01	TUG-T100	2023 Jul 26	g'	100	5.31	AIRMASS
5938.01	TUG-T100	2023 Sep 07	r'	100	7.93	Sky/Pixel_T1
5938.01	SAINT-EX	2024 Sep 26	z_s'	13	4.09	SKYLEVEL, FWHM_x
5938.01	ARTEMIS	2024 Jul 27	g'	11	2.80	FWHM
5938.01	ARTEMIS	2024 Sep 23	z_s'	10	3.87	–
5938.01	LCO-TEID−1m0	2023 Aug 04	i'	20	3.89	–
5938.01	ULMT	2023 Jun 25	r'	60	5.51	–
5938.01	TJO-0m8	2024 Sep 14	g'	75	3.96	–
7009.01	*TESS*	84, (56, 57, 74, 75, 76, 81, 82)[a]	*TESS*	120 (200)[a]	>21	GP: Matérn-3/2 + Jitter [b]
7009.01	MuSCAT2	2025 Mar 21	g', r', i', z_s'	60, 60, 15, 60	6.96	–
7009.01	LCO-TEID−1m0	2024 Jul 09	i'	95	3.128	Width_T1, BJD_TDB

[a]The QLP/HSLP sectors and exposure times are reported in parenthesis.
[b]Independent GP parameters were fitted to the PDCSAP and QLP/HSLP light curves.

Teide Observatory in Tenerife (N. Narita et al. 2019). It observes simultaneously in the Sloan g', r', i', and z_s' bands, with a field of view of approximately 7.4 arcmin × 7.4 arcmin and a pixel scale of 0.435 arcsec.

We observed full transits of TOI-2133.01 on 2025 May 30 UT, TOI-5734.01 on 2025 March 18 UT, and TOI-7009.01 on 2025 March 21 UT. Exposure times were independently set for each detector based on the target brightness and observing conditions. They ranged from 4–10 s for TOI-2133 and TOI-5734, and 15–60 s for TOI-7009. Focus was adjusted before and/or during the observations to maximize efficiency and avoid saturation.

The MuSCAT2 data were reduced using a dedicated pipeline (H. Parviainen et al. 2020), which optimized comparison star selection and aperture sizes for extracting the target's photometric time series. The chosen target apertures were 4.35, 10.875, and 5.655 arcsec for TOI-2133, TOI-5734, and TOI-7009, respectively, with comparison star apertures ranging from 1.74 to 8.265 arcsec.

2.2.2 *LCOGT-1m0*

We used the Las Cumbres Observatory Global Telescope (LCOGT; T. M. Brown et al. 2013) 1.0m network to observe TOI-2133.01, TOI-5734.01, TOI-5938.01, and TOI-7009.01. The telescopes are equipped with the 4096 × 4096 SINISTRO detectors having a pixel scale of 0.389 arcsec and a field-of-view of 26 arcmin × 26 arcmin. TOI-2133.01 was observed at the Southern African Astronomical Observatory (SAAO) node on UTC 2024 May 7 in the Sloan-i' filter. TOI-5734.01 was observed at Teide Observatory node on UTC 2023 December 11 in the Pan-STARRS z_s filter. TOI-5938.01 was observed at Teide Observatory node on UTC 2023 August 04 in the Pan-STARRS z_s filter. TOI-7009.01 was carried out at Teide Observatory node on UTC July 9, 2024, in the Sloan-i' filter. All science data were calibrated using the standard LCOGT `BANZAI` pipeline (C. McCully et al. 2018), and photometric extraction was performed using the AstroImageJ (AIJ) software (K. A. Collins et al. 2017).

2.2.3 *TUG-T100*

We observed two full transits of TOI-5938.01 with the 1 m Turkish telescope T100 on 2023 July 26 and 2023 September 07, using the g' and r' filters, respectively. The telescope is located at the Bakırlıtepe/Antalya campus of the Türkiye National Observatories (TUG) at an altitude of 2500 m and is equipped with a cryo-cooled SI 1100 CCD, which has 4096 × 4096 pixels and a FoV of 21 arcmin × 21 arcmin. We used the 2 × 2 binning mode to reduce the readout time from 45 to 15 s, and we utilized the defocusing technique (J. Southworth et al. 2009) to improve photometric precision. The data reduction and differential photometry relative to a synthetic star created by summing a set of comparison stars were performed using the AIJ software (K. A. Collins et al. 2017).

2.2.4 *SAINT-EX and ARTEMIS*

SAINT-EX observatory (B. O. Demory et al. 2020), located at the Sierra de San Pedro Mártir (México), and SPECULOOS-North (so called ARTEMIS; A. Y. Burdanov et al. 2022), installed at Tenerife Observatory (Spain), are equipped with a 2K×2K Andor iKon-L detector having a field-of-view of 12 arcmin × 12 arcmin and a pixel scale of 0.35 arcsec pixel^{-1}. Both SAINT-EX and ARTEMIS are twins of the SPECULOOS-South observatory (E. Jehin et al. 2018; D. Sebastian et al. 2021), located at ESO Paranal (Chile). With these facilities, we observed the TOI-5938.01 candidate, using the Sloan-g' and -z' filters. Data processing and photometric measurements were performed using the `PROSE` [4] pipeline (L. J. Garcia et al. 2022).

[4]`Prose`: https://github.com/lgrcia/prose

Downloaded from academic.oup.com/mnras/article/549/3/stag183/8442244 by UNIV LEIGE FAC PSYCH SCIENCES L'EDUCATION user on 26 November 2026

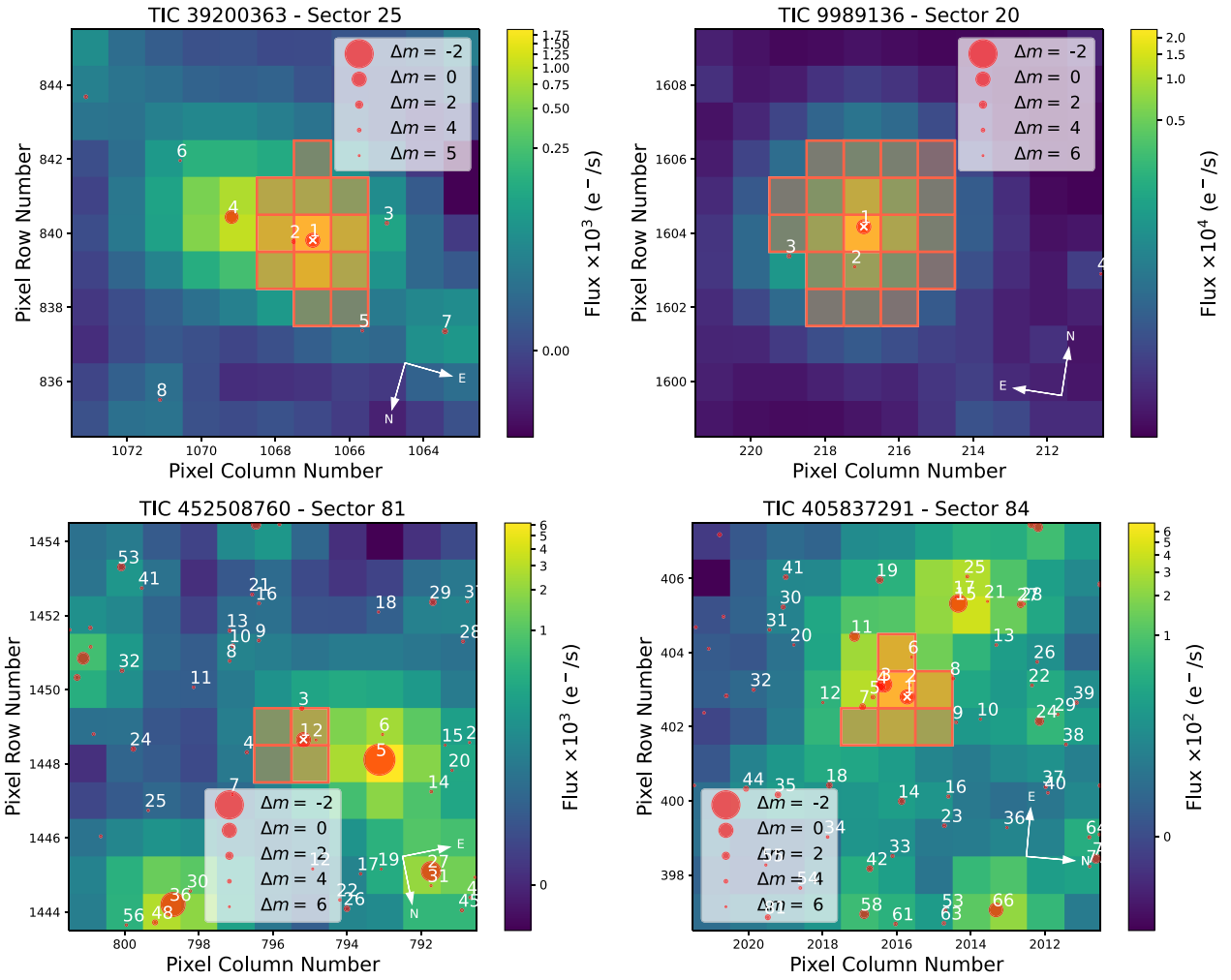


Figure 1. Representative *TESS* TPF images of TOI-2133 (top left), TOI-5734 (top right), TOI-5938 (bottom left), and TOI-7009 (bottom right). The pixels highlighted in red denote the aperture mask used to calculate the SAP. The red circles represent neighbouring sources listed in *Gaia* DR3, the target star being marked with a white 'x' and identifier 1. The size of the red circles is inversely proportional to the apparent magnitude difference with respect to the target star. The maximum contrast magnitude of the plotted sources is $\Delta m = 6$ mag.

2.2.5 TJO

A transit of TOI-5938.01 was observed in 2024 September 14 using the 0.8m Joan Oró telescope (TJO; J. Colomé et al. 2010) at the Montsec Observatory (Lleida, Spain; 4h of total observing time, per-point precision of 2680 ppm at 1.25 min cadence; g' filter observations, refining the check on chromaticity). We obtained a total of 170 images with an exposure time of 75 s, using the g' filter of the LAIA imager, a 4k×4k CCD with a field of view of 30 arcmin and a 0.4 arcsec pixel^{-1} scale. The TJO CCD images were calibrated with darks, bias, and flat fields with the ICAT pipeline (J. Colome & I. Ribas 2006). The differential photometry was extracted with AIJ (K. A. Collins et al. 2017) using the aperture size that minimized the rms of the resulting relative fluxes and a selection of the brightest comparison stars in the field that did not show variability.

2.2.6 ULMT

We observed a full transit window of TOI-5938.01 on *UT* June 25, 2023 in the Sloan r' band from the 0.61-m University of Louisville Manner Telescope (ULMT) located at Steward observatory near Tucson, AZ. Its 9576 × 6388 ASI6200 camera with a cooled Sony IMX455 sensor and an image scale of 0.165 arcsec per pixel, resulting in a 26.3 arcmin × 17.6 arcmin FoV. With an exposure of 60 s, 160 images were acquired with a cadence of 66 s. After dark subtraction, WCS calibration was added to each image using Astrometry.net (D. Lang et al. 2010) code. With apertures placed by Gaia DR3 coordinates allowing for proper motion, photometric data were extracted and BJD times were computed with the AIJ. Light curves were obtained for the target star and for all known *Gaia* DR3 and TICv8 neighbouring stars within 2.5 arcmin of TOI-5938 that are bright enough in the *TESS* band to produce the *TESS* detection (allowing for an extra 0.5 mag fainter). We calculate the RMS of each of the light curves in 5 min bins to identify those that are larger by factors of 3 to 5 than the depth expected if each respective star were to be the cause of the TOI-5938.01 detection in *TESS* data. We then also visually inspected all of the light curves to ensure that there were no obvious deep eclipse-like signals, irrespective of the RMS test. We therefore rule out a near eclipsing binary blend within nearby bright stars as the cause of the TOI-5938.01 detection in the *TESS* data. Using

Downloaded from academic.oup.com/mnras/article/549/3/stag183/8442244 by UNIV LEIGE FAC PSYCH SCIENCES L'EDUCATION user on 26 November 2026

a circular photometric aperture with a 5.5 arcsec radius centered on TOI-5938, a transit-like event was detected on-target, and we find a depth of 3.1 ppt with an RMS of 0.65 binned into 5-min intervals in a preliminary analysis.

2.2.7 CHEOPS

CHEOPS is a 30-cm space telescope in a nadir-locked sun-synchronous low-earth orbit focussed on the characterization of transiting exoplanets (W. Benz et al. 2021). TOI-5734 was observed by *CHEOPS* as part of the ChATeAUX (Cheops And Tess vAlidate Unconfirmed eXoplanets) programme on 2023-02-23 (filekey CH_PR130056_TG009701_V0300) which caught a clear egress. This programme was designed to observe short flexible observations of the transits of *TESS* candidates in order to assist with their radius determination, ephemeris and multicolour photometric variation. The data was reduced using the `chexoplanet` package[5] (see e.g. J. A. Egger et al. 2024) which combines PSF photometry (using `PIPE` [6]), a cubic bspline fitted to rollangle variations, and linear decorrelation against housekeeping parameters to produce accurate transit photometry robust to intrument systematics.

2.3 Spectroscopy

2.3.1 FLWO/TRES

High-resolution spectra of the stars were obtained using the Tillinghast Reflector Echelle Spectrograph (TRES; G. Fűrész 2008) installed on the 1.5-m telescope at the Fred Lawrence Whipple Observatory (FLWO) in Arizona, USA. TRES is an optical (3900–9100 Å), fiber-fed echelle spectrograph that delivers a resolving power of approximately 44 000. The spectra are part of the TFOP[7] for reconnaissance spectroscopy (A. Bieryla et al. 2023), and therefore, have modest signal-to-noise ratios. Data reduction and spectral extraction followed the procedures outlined in L. A. Buchhave et al. (2010).

2.3.2 IRTF/SpeX

We obtained near-infrared spectroscopy of TOI-5938 on 18 May 2025 using the SpeX spectrograph (J. T. Rayner et al. 2003) mounted on the 3.2-m NASA Infrared Telescope Facility (IRTF). Observations were carried out in the short-wavelength cross-dispersed (SXD) mode with the 0.3 arcsec × 15 arcsec slit, which was aligned along the parallactic angle. The sky was clear, with an average seeing of ∼0.8 arcsec.

Six science exposures were acquired following an ABBAAB nodding sequence with 200 s integration time, bracketed by 20 s integrations of the A0 V telluric standard HD 192538 ($V = 6.5$) and the standard SXD calibration set. Both target and telluric standard were observed at an airmass of ∼1.0. Data reduction was performed with Spextool v4.1 (M. C. Cushing, W. D. Vacca & J. T. Rayner 2004), as implemented in previous studies (K. Barkaoui et al. 2023, 2024, 2025b M. Ghachoui et al. 2023, 2024).

The extracted spectrum spans 0.80–2.44 μm with a resolving power of $R \sim 2000$, corresponding to approximately 2.5 pixels per resolution element, and a median per-pixel signal-to-noise ratio of 176 (Fig. 3).

[5]https://github.com/hposborn/chexoplanet
[6]https://github.com/alphapsa/PIPE
[7]https://tess.mit.edu/followup

2.4 High-resolution imaging

2.4.1 2.5m-SAI

High-angular-resolution images of TOI-5938 were obtained on 2023 August 31 with the speckle polarimeter mounted on the 2.5-m telescope at the Caucasian Observatory of the Sternberg Astronomical Institute (Lomonosov Moscow State University). The observations employed a low-noise Hamamatsu ORCA-Quest CMOS detector (I. A. Strakhov, B. S. Safonov & D. V. Cheryasov 2023) in the I_c band, achieving a diffraction-limited angular resolution of 0.083 arcsec. Atmospheric conditions were excellent, with a long-exposure seeing of 0.53 arcsec. No nearby stellar companions were detected. From these data, we derived contrast limits of $\Delta I_c = 3.8$ mag at 0.25 arcsec and 7.3 mag at 1.0 arcsec from the target. The reconstructed image and corresponding contrast curve are presented in Fig. A1.

2.4.2 5m-Palomar

Observations of TOI-2133, TOI-5734, and TOI-5938 were conducted with the PHARO instrument (T. L. Hayward et al. 2001) on the Palomar Hale (5m) behind the P3K natural guide star AO system (R. Dekany et al. 2013) on March 3 (2021), November 27 (2023), and June 29 (2023), respectively.

The scale for PHARO is 0.025 arcsec per pixel. The data were collected in a standard 5-point quincunx dither pattern. The calibrated data were combined into a single mosaic frame, resulting in a final resolution of ∼0.1 arcsec.

To assess the detection limits in the final co-added AO frames, we performed source injection experiments by placing artificial companions azimuthally around the target star at intervals of 20°, and at radial distances corresponding to integer multiples of the stellar PSF FWHM (E. Furlan et al. 2017). For each location, the flux of the injected companion was scaled until it reached a 5σ detection level as determined through standard aperture photometry. The contrast limit at a given separation was then defined as the average 5σ detection threshold over all azimuthal positions, with the associated uncertainty derived from the RMS scatter of these measurements. Within these sensitivity limits, no nearby background sources are detected. These observations, along with the contrast curves, are displayed in Fig. A2.

2.4.3 WIYN observations

TOI-7009 was observed on 2024 September 13 with the NN-EXPLORE Exoplanet Stellar Speckle Imager (NESSI; N. J. Scott et al. 2018) at the WIYN Observatory on Kitt Peak. NESSI simultaneously acquired 9000 short-exposure speckle images in two bandpasses centred at 562 and 832 nm. The effective field of view was restricted to 4.6 arcsec × 4.6 arcsec by reading out a 256 × 256 pixel subarray of the EMCCD detectors centred on the target. Photometric analysis was limited to separations within 1.2 arcsec of the target star. A nearby point-source calibrator was also observed to characterize the PSF; the calibration consisted of a single 1000-frame image set used for speckle reconstruction.

The data were reduced using the NESSI pipeline described by S. B. Howell et al. (2011), which produces reconstructed images in each filter and corresponding contrast curves. The contrast limits were determined from the spatial variation of the noise in the reconstructed images as a function of angular separation. No

Downloaded from academic.oup.com/mnras/article/549/3/stag183/8442244 by UNIV LEIGE FAC PSYCH SCIENCES L'EDUCATION user on 26 November 2026

Table 2. Stellar parameters.

Parameter	TOI-2133	TOI-5734	TOI-5938	TOI-7009
TIC ID	39 200 363	9989 136	452 508 760	405 837 291
		Astrometric [a]		
RA (epoch 2015.5)	17:24:58.52	07:25:01.4	20:15:38.12	19:58:03.15
DEC (epoch 2015.5)	+32:47:54.23	+37:13:52.04	+28:39:33.21	+55:39:03.7
$\mu_{\rm RA}$ (mas yr^{-1})	-17.882 ± 0.036	-27.643 ± 0.102	-78.870 ± 0.041	-36.065 ± 0.028
$\mu_{\rm DEC}$ (mas yr^{-1})	64.347 ± 0.036	14.349 ± 0.083	-76.991 ± 0.044	5.946 ± 0.027
Distance (pc)	75.20 ± 0.14	32.51 ± 0.08	114.04 ± 0.37	184.12 ± 0.47
		Photospheric and physical [b]		
$T_{\star,\rm eff}$ (K)	4250 ± 45	4790 ± 50	4650 ± 50	4080 ± 25
$\log g_\star$ (dex)	4.60 ± 0.14	4.59 ± 0.09	4.59 ± 0.08	4.63 ± 0.12
$[{\rm Fe/H}]_\star$ (dex)	-0.01 ± 0.08	-0.09 ± 0.04	0.07 ± 0.04	-0.11 ± 0.06
$R_\star$ ($R_\odot$)	0.620 ± 0.019	0.708 ± 0.020	0.712 ± 0.018	0.564 ± 0.016
$M_\star$ ($M_\odot$)	0.644 ± 0.019	0.736 ± 0.017	0.744 ± 0.016	0.583 ± 0.014
		Magnitudes [a]		
V	12.008 ± 0.046	9.613 ± 0.006	12.310 ± 0.046	14.161 ± 0.126
TESS	10.857 ± 0.006	8.545 ± 0.006	11.352 ± 0.006	12.934 ± 0.006
J	9.759 ± 0.022	7.613 ± 0.019	10.327 ± 0.024	11.815 ± 0.021
K_s	9.003 ± 0.018	6.987 ± 0.016	9.618 ± 0.023	11.005 ± 0.025

[a] From the *TESS* Input Catalogue (TIC).
[b] Determined in this work.

nearby companion sources were detected in either bandpass. The reconstructed images and contrast curves are shown in Fig. A3.

3 STELLAR CHARACTERIZATION

3.1 FLWO/TRES

3.1.1 SPC

Stellar atmospheric parameters from TRES spectra are available on the Exoplanet Follow-up Observing Programme (ExoFOP[8]) website and were derived using the *Stellar Parameter Classification* (SPC; L. A. Buchhave et al. 2012; A. Bieryla et al. 2021) tool, which cross-correlates the observed spectra with a grid of synthetic models based on Kurucz atmospheric models (R. L. Kurucz 1992). The analysis focuses on the 5050–5360 Å range, covering effective temperatures from 3500 to 9750 K, surface gravities between 0.0 and 5.0 dex, metallicities from −2.5 to +0.5 dex, and projected rotational velocities up to 200 km s^{-1}. The cross-correlation peak provides a measure of fit quality, with surface gravity priors informed by Yonsei–Yale isochrones. Minimum uncertainties of 50 K in $T_{\star,\rm eff}$, 0.08 dex in $[{\rm Fe/H}]_\star$, and 0.1 dex in $\log g_\star$ are imposed to account for systematic model errors. Only reliable SPC measurements are reported to ExoFOP-*TESS*.

3.1.2 ZASPE

We derived the stellar atmospheric parameters using the *Zonal Atmospheric Stellar Parameter Estimator* (ZASPE; R. Brahm et al. 2017). We used blaze-corrected spectra obtained with the TRES spectrograph, formatted in the three-column ASCII structure required by ZASPE (echelle order, wavelength, flux) and restricted to the 5000–6000 Å range, which maximizes sensitivity to atmospheric parameters. ZASPE models the observed spectrum by fitting it against a grid of synthetic spectra. Among the available grids, we adopted the one based on the *Kurucz* model atmospheres (F. Castelli & R. L. Kurucz 2003), as described in R. Brahm et al. (2017), which ensures optimal performance with the code. ZASPE identifies and fits spectral regions most sensitive to the parameters of interest, deriving the effective temperature ($T_{\rm eff}$), surface gravity (log g), metallicity ([Fe/H]), and projected rotational velocity (v sin i) via least-squares minimization against the synthetic grid. Parameter uncertainties are estimated through ZASPE's internal Monte Carlo routine, which assumes that the principal source of error arises from the systematic mismatch between the observed spectrum and the best-fitting synthetic spectrum. When multiple spectra were available, we computed weighted averages of the parameters from each individual spectrum, using the spectral SNR as weights. We used the ISOCHRONES package (T. D. Morton 2015), with the ZASPE spectroscopic parameters and broad-band photometry as inputs, to estimate the stellar masses, radii, and mean densities. The final stellar parameters adopted in this study are reported in Table 2.

3.2 IRTF/SpeX

We analysed the SpeX SXD spectrum of TOI-5938 using the SpeX Prism Library Analysis Toolkit (SPLAT; A. J. Burgasser & Splat Development Team 2017), following previous SpeX analyses (e.g. L. Delrez et al. 2022; A. H. M. J. Triaud et al. 2023; M. Gillon et al. 2024; M. Timmermans et al. 2024). Comparison to spectral standards in the the IRTF Spectral Library (M. C. Cushing, J. T. Rayner & W. D. Vacca 2005; J. T. Rayner, M. C. Cushing & W. D. Vacca 2009) yields a strong match to the K5 V standard HD 36003. We adopt a near-infrared spectral type of K5.0 ± 1.0 accordingly. Based on the H_2O–K_2 index (B. Rojas-Ayala et al. 2012) and K-band atomic features of Na I and Ca I, we estimate a stellar iron abundance of $[{\rm Fe/H}] = -0.16 \pm 0.11$ using the relation from A. W. Mann et al. (2013), consistent with a solar metallicity.

[8] https://exofop.ipac.caltech.edu/tess/

Downloaded from academic.oup.com/mnras/article/549/3/stag183/8442244 by UNIV LEIGE FAC PSYCH SCIENCES L'EDUCATION user on 26 November 2026

4 METHODS

We employed three complementary approaches to investigate the planetary nature of the candidates, which are described in the following subsections.

4.1 Multicolour photometry

First, we used multicolour photometry (H. Parviainen et al. 2019) to search for wavelength-dependent transit depth variations, which can reveal flux contamination from a third light source affecting the apparent radius or indicate a blended eclipsing binary. This method enables us to marginalize the true radius of the transiting object over contamination scenarios consistent with the observed photometry and stellar parameters. True radius values below 0.8 R_J fall beneath the brown dwarf regime (A. Burrows et al. 2001), supporting the classification of the transiting object as a planet. Following A. Peláez-Torres et al. (2024), we define the false positive probability (FPP) as the fraction of the radius posterior distribution exceeding the said threshold, and consider candidates fully validated when FPP $<$ 1 per cent. This FPP is inherently conservative, as the size limit works only in one direction, ruling out stellar or brown dwarf companions if the radius is below the threshold, but it cannot exclude the planetary nature of larger objects. Consequently, the multicolour photometry method is inconclusive for validating giant planets.

In practice, we simultaneously fitted all photometric light curves with a contamination transit model and baseline treatment analogous to those adopted by G. Morello et al. (2023). The contamination transit model is defined as

$$\hat{F}(t) = (1-\beta)(1-\Lambda(t)) + \beta, \tag{1}$$

where $1-\Lambda(t)$ represents the pure planetary transit model, and

$$\beta = \frac{F_c}{F_\star + F_c}, \tag{2}$$

with $F_\star$ and F_c denoting the flux from the target star and the contaminating sources, respectively. The pure transit model $\Lambda(t)$ was generated using a modified version of the `pylightcurve` package (A. Tsiaras et al. 2016), assuming circular orbits and a power-2 limb-darkening law (D. Hestroffer 1997; G. Morello et al. 2017).

For ground-based observations, we assumed that F_c originates from a single blended star. We computed the passband-integrated fluxes $F_\star$ and F_c from a grid of PHOENIX stellar atmosphere models (T. O. Husser et al. 2013; A. Claret 2018) using the `ExoTETHyS.BOATS` subpackage (G. Morello et al. 2021), as a function of effective temperature and surface gravity. For the target star, $T_{\star,\rm eff}$ and $\log g_\star$ were fixed to their estimated values, while for the contaminant, $T_{c,\rm eff}$, $\log g_c$, and a relative flux scaling factor f_c were treated as free parameters. Due to their larger pixel scales, we fitted independent contamination parameters, β, for the *TESS* and *CHEOPS* observations. To account for systematics in the *TESS* data, we employed Gaussian Process (GP) regression with a Matérn-3/2 kernel using the `celerite` package (D. Foreman-Mackey et al. 2017). Ground-based light curves were detrended simultaneously by fitting linear baseline models based on auxiliary variables, as detailed in Table 1. The *CHEOPS* data were used as pre-detrended. Figs 2 and C1–C2 shows the detrended light-curves and best fit model from *TESS* and follow-up photometry, respectively.

We adopted uniformative priors for the majority of light-curve fitting parameters (see Table C1). To help constrain transit timings in lower quality data sets, we adopted Gaussian priors on the orbital period and transit epoch, centred on the ExoFOP values with uncertainties inflated by a factor of three. We further assumed stellar density priors derived from spectroscopy (see Section 3). The priors on the power-2 limb-darkening coefficients were derived from the stellar parameters $T_{\star,\rm eff}$, $\log g_\star$ using `ExoTETHyS.SAIL` (G. Morello et al. 2020a, b) and the previously mentioned PHOENIX grid, with uncertainties set to five times the largest passband standard deviation. Negative contamination parameters were allowed to account for potential systematic errors, such as overcorrection of background or blends, and to avoid boundary-induced bias (e.g. the classic Lucy–Sweeney effect; L. B. Lucy & M. A. Sweeney 1971).

4.2 Statistical validation

Secondly, we conducted a statistical validation employing the TRICERATOPS software package (see, e.g. S. Giacalone et al. 2021, 2022). This methodology evaluates the relative probabilities of various astrophysical scenarios that could account for the observed signal, integrating *TESS* photometry, *Gaia* astrometric and photometric data, high-resolution imaging contrast curves, and models of the Galactic stellar population. TRICERATOPS differentiates between validated planets, likely planetary candidates, and nearby false positives by computing two principal parameters: the FPP, which quantifies the probability that a candidate is a false positive, and the Nearby FPP (NFPP), which estimates the likelihood that the detected signal originates from a nearby contaminant. These probabilities are interpreted according to established thresholds: candidates with FPP $<$ 0.015 and NFPP $<$ 0.001 are classified as validated planets; those with FPP $<$ 0.5 and NFPP $<$ 0.001 are considered likely planetary candidates; and those with NFPP $>$ 0.1 are identified as probable nearby false positives. In this study, we utilized *TESS* photometric data as detailed in Section 2.1, along with high-resolution imaging curves acquired using the 5-m Palomar Observatory, as described in Section 2.4.2. Additionally, the transit events associated with TOI-2133.01, TOI-5734.01, TOI-5938.01, and TOI-7009.01 were all identified via ground-based photometry. Consequently, for each of these cases, the NFPP was determined to be zero.

4.3 Neural network-based statistical vetting with WATSON-Net

To complement our validation efforts, we applied WATSON-Net, a neural network composed of convolutional branches designed to classify transit-like signals as either planetary or false positives. The model was trained on a labeled data set of Kepler TCEs, comprising both confirmed exoplanets and known astrophysical false positives, using as inputs the phase-folded light curves and a set of diagnostic features extracted from SPOC pipeline products. The architecture and training methodology are described in detail in M. Dévora-Pajares et al. (2025). WATSON-Net outputs a continuous score between 0 and 1, representing the likelihood that a given signal corresponds to a true transiting exoplanet. Thresholds for interpreting these scores were empirically calibrated on independent test sets. For Kepler signals, we adopted a threshold of 0.646 for the classification of a signal as a *Likely Planet*, and 0.961 for classification as a *Validated Planet*. Due to differences in photometric precision, contamination environment, and vetting

Downloaded from academic.oup.com/mnras/article/549/3/stag183/8442244 by UNIV LEIGE FAC PSYCH SCIENCES L'EDUCATION user on 26 November 2026

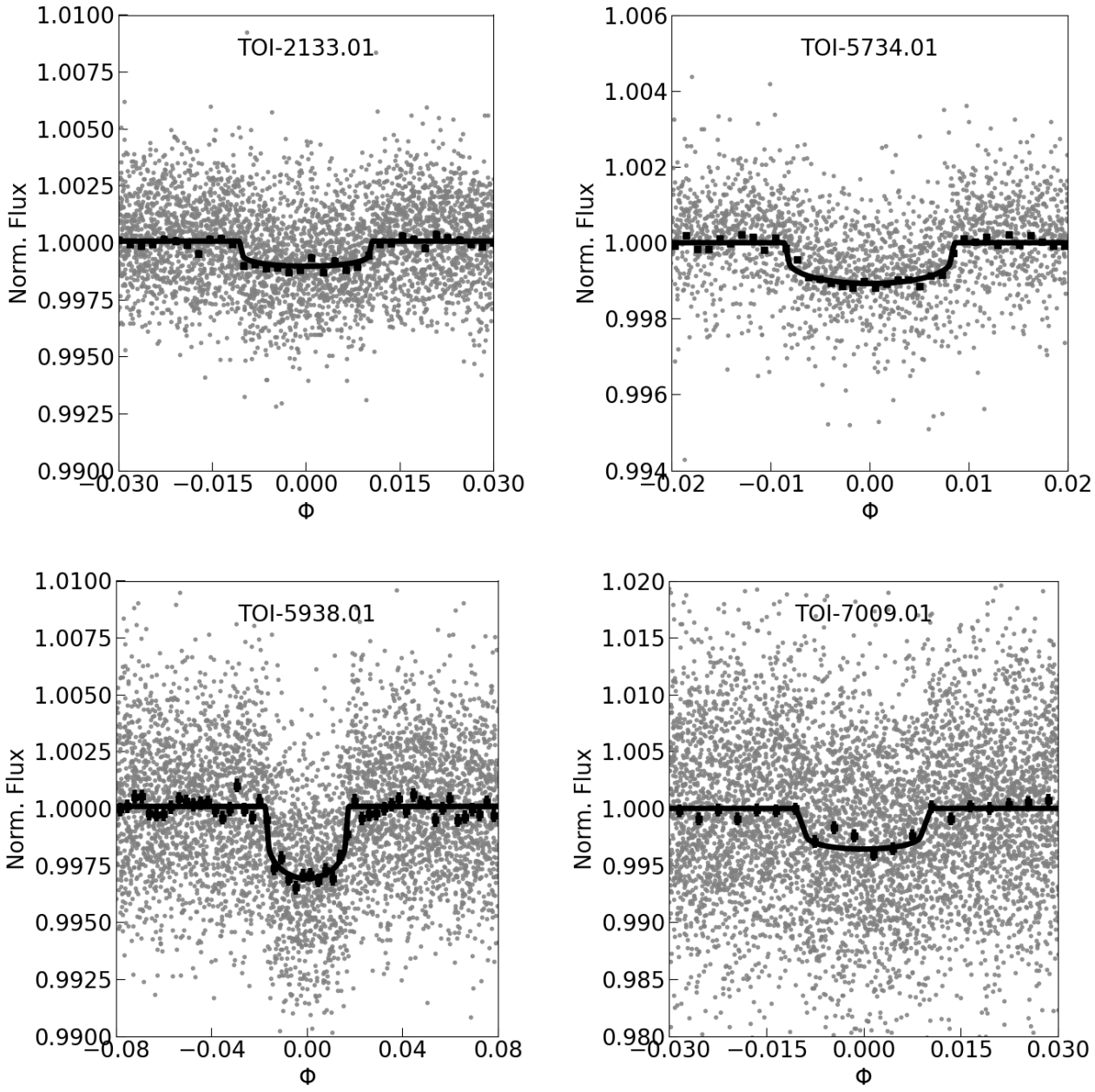


Figure 2. Phase-folded, detrended *TESS* light curves of TOI-2133.01 (top left), TOI-5734.01 (top right), TOI-5938.01 (bottom left), and TOI-7009.0 (bottom right). For clarity, 10-min bins (with error bars) and the best-fitting transit model are overlaid.

completeness, which led to different distributions of probabilities, a stricter threshold of 0.997 was adopted for *TESS* targets to assign the *Validated Planet* label.

It is important to note that from the scores reported by WATSON-Net, there are no equivalencies to FPP values as derived from Bayesian validation frameworks, such as for the multicolour photometry method and TRICERATOPS. Instead, they represent the calibrated confidence of the neural network in classifying a signal as planetary, based on the training distribution and diagnostic features. As such, they should be interpreted as complementary statistical evidence rather than direct estimates of astrophysical FPP.

4.4 Final transit modelling and parameter estimation

After candidate validation, we repeated the simultaneous fitting of the same light-curves as in Section 4.1, modifying the contamination model by omitting some or all terms to derive the final planetary and orbital parameters. In particular, we tested variants of the fit omitting the colour contaminant in the ground-based photometry, while retaining the *TESS* and/or CHEOPS blend terms or assuming no contamination. Model selection was based on the Akaike Information Criterion (AIC, H. Akaike 1974), with preference for the simplest model whose AIC was within 2 units of the minimum. We also tested alternative fits allowing for eccentric orbits and/or using uniform stellar-density priors.

Downloaded from academic.oup.com/mnras/article/549/3/stag183/8442244 by UNIV LEIGE FAC PSYCH SCIENCES L'EDUCATION user on 26 November 2026

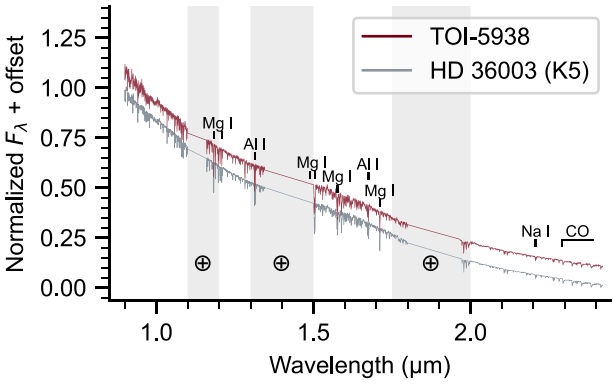


Figure 3. SpeX SXD spectrum of TOI-5938 alongside the K5 V standard HD 36003. Strong spectral features of K dwarfs are noted, and regions of high telluric absorption are shaded.

5 RESULTS

5.1 Validated planets

Table 3 summarizes the validation metrics for the four TOI candidates, including the FPPs from multicolour photometry (MC) and statistical validation (SV), as well as the WATSON-Net classification scores. These metrics provide independent assessments of the planet-like nature of each candidate.

Multicolour photometry provides the strongest support in favour of three targets: TOI-5734.01, TOI-5938.01, and TOI-7009.01, with FPP (MC) values significantly below the 0.01 threshold. In particular, they exhibit exceptionally low FPPs (MC) of $(2.6 \pm 2.6) \times 10^{-8}$, $(8.4 \pm 1.5) \times 10^{-7}$, and $(2.6 \pm 2.6) \times 10^{-8}$, respectively, indicating near-certain planetary interpretations. The FPP (MC) for TOI-2133.01 is formally quite high. However, a closer inspection reveals that the larger radii are associated with a secondary peak in the posterior distribution, corresponding to a highly contaminated but colour-independent solution (see Table 4 and Fig. C3). Values of $R_p > 0.8\,R_J$ for TOI-2133.01 are only obtained when $\beta_{TESS} > 92$ per cent, i.e. when most of the flux within the *TESS* aperture is assumed to come from a blended source of similar spectral type as the candidate host star. This scenario is very unlikely, also given the constraints from high-resolution images.

TRICERATOPS obtained FPP (SV) values of $(2.8 \pm 0.3) \times 10^{-3}$, $(2.6 \pm 0.4) \times 10^{-3}$, $(5.0 \pm 1.0) \times 10^{-4}$, and $(9.7 \pm 2.0) \times 10^{-3}$ for TOI-2133.01, TOI-5734.01, TOI-5938.01, and TOI-7009.01, respectively. The first three candidates have robust validations, with their 3σ upper bounds remaining well below the 0.01 threshold. TOI-7009.01 also satisfies the nominal validation criterion, although its confidence level (at $\sim 2.6\sigma$) is less stringent than for the other systems, and the inclusion of seven QLP/HSLP 200-s sectors was decisive in decreasing the FPP (SV).

The WATSON-Net score for TOI-2133 is 0.998 ± 0.005, exceeding the *TESS* validation threshold, and thus qualifying as a *Validated Planet* according to the model. TOI-5734 received a score of 0.996 ± 0.007, narrowly missing the validation threshold by less than 1σ, and is therefore considered a *Likely Planet* with very high confidence. TOI-5938, with a score of 0.983 ± 0.018, also falls below the validation threshold but remains well above the *Likely Planet* boundary. Despite its slightly larger uncertainty, this score remains below 1σ of the validation threshold, indicating strong statistical consistency with the population of true exoplanets observed during training. Finally, TOI-7009.01 obtained a score of 0.897 ± 0.305, placing it in the *Likely Planet* regime but with substantial uncertainty. The inclusion of seven additional QLP/HSLP 200-s sectors significantly increases the WATSON-Net score relative to the single available *TESS* SPOC sector; however, the score remains inconclusive, partly due to the limited metadata available for the QLP/HSLP products (e.g. centroid time series and difference images).

In summary, the four TOI candidates are supported as planetary in nature by at least two complementary methods, with the third method also indicating a planetary interpretation but not meeting the formal validation threshold. All satisfy the classical statistical validation criterion, with multicolour photometry providing strong additional evidence in the form of near-zero FPPs (MC), except for TOI-2133.01. The high FPP (MC) for TOI-2133.01 arises from an improbable scenario, which can be confidently ruled out using other available data. Taken together, the agreement between multiple independent diagnostics reduces the likelihood of false-positive interpretations compared to reliance on a single method (e.g. J. N. Winn & G. Stefánsson 2025). Finally, we classify TOI-2133 b, TOI-5734 b, TOI-5938 b, and TOI-7009 b as newly validated planets.

5.2 System parameters

Table 5 reports the final parameters for the four systems, including those fitted or derived from the transit analysis, the stellar parameters determined spectroscopically, and the planetary and orbital parameters obtained by combining both. The planetary masses and stellar radial-velocity semi-amplitudes are predicted using `SPRIGHT` (H. Parviainen, R. Luque & E. Palle 2024), adopting the theoretical mass–radius relations of L. Zeng et al. (2019) for FGK host stars.

For none of the four planets is the all-terms contamination model favoured by the AIC across the different contamination scenarios, owing to the lack of colour dependence in the ground-based photometry.

For TOI-2133 b, the model including a free β_{TESS} term is favoured over the contamination-free scenario, with $\Delta\mathrm{AIC} = -10.6$. The corresponding $\beta_{TESS} = 0.25 \pm 0.07$, and neglecting this term (i.e. adopting the contamination-free fit) reduces the

Table 3. Summary of validation metrics for each target, including FPPs from multicolour photometry (MC) and statistical validation (SV), and the WATSON-Net score. The final classification is also reported.

Parameter	TOI-2133.01	TOI-5734.01	TOI-5938.01	TOI-7009.01
FPP (MC)	0.08597 ± 0.00005	$\mathbf{(2.6 \pm 2.6) \times 10^{-8}}$	$\mathbf{(8.4 \pm 1.5) \times 10^{-7}}$	$\mathbf{(2.6 \pm 2.6) \times 10^{-8}}$
FPP (SV)	$\mathbf{(2.8 \pm 0.3) \times 10^{-3}}$	$\mathbf{(2.6 \pm 0.4) \times 10^{-3}}$	$\mathbf{(5.0 \pm 1.0) \times 10^{-4}}$	$\mathbf{(9.7 \pm 2.0) \times 10^{-3}}$
WATSON-Net	$\mathbf{0.998 \pm 0.005}$	0.996 ± 0.007	0.983 ± 0.018	0.897 ± 0.305

Note. The values in bold exceed the nominal thresholds for validation: <0.01, <0.01, and >0.997, respectively.

Downloaded from academic.oup.com/mnras/article/549/3/stag183/8442244 by UNIV LEIGE FAC PSYCH SCIENCES L'EDUCATION user on 26 November 2026

Table 4. Best-fitting transit and contamination parameters.

Parameter	TOI-2133.01	TOI-5734.01	TOI-5938.01	TOI-7009.01
		Transit (fitted)		
$R_p/R_\star$	$0.0354^{+0.0606}_{-0.0028}$	0.0363 ± 0.0012	$0.0503^{+0.0015}_{-0.0012}$	$0.0611^{+0.0043}_{-0.0048}$
P (d)	$3.8266476^{+4.5e-6}_{-4.1e-6}$	$6.1842158^{+5.4e-6}_{-6.5e-6}$	$2.2604244^{+3.7e-6}_{-3.4e-6}$	$2.3206611^{+4.2e-6}_{-4.3e-6}$
T_0 (BTJD)	$1985.8829^{+0.0013}_{-0.0016}$	$1848.6878^{+0.0018}_{-0.0016}$	$2820.1814^{+0.0010}_{-0.0011}$	3392.3627 ± 0.0005
$\rho_\star$ ($\rho_\odot$)	$2.63^{+0.20}_{-0.14}$	$2.19^{+0.16}_{-0.20}$	$2.11^{+0.11}_{-0.15}$	3.27 ± 0.21
b	$0.14^{+0.12}_{-0.09}$	$0.25^{+0.11}_{-0.14}$	$0.20^{+0.10}_{-0.12}$	$0.745^{+0.018}_{-0.017}$
		Contaminant (fitted)		
$T_{c,\mathrm{eff}}$	3869^{+417}_{-1391}	2750^{+1684}_{-357}	2610^{+926}_{-240}	2795^{+1120}_{-388}
$\log g_c$	unconstrained	unc.	unc.	unc.
f_c	$0.12^{+8.03}_{-1.36}$	$0.84^{+0.84}_{-0.99}$	$1.76^{+2.71}_{-1.32}$	$0.30^{+2.46}_{-0.86}$
β_{TESS}	$0.30^{+0.60}_{-0.16}$	$0.36^{+0.06}_{-0.07}$	$-0.03^{+0.08}_{-0.07}$	$0.05^{+0.19}_{-0.24}$
$\beta_{\mathrm{QLP/HSLP}}$	–	–	–	$0.20^{+0.12}_{-0.16}$
β_{CHEOPS}	–	$0.37^{+0.05}_{-0.06}$	–	–
		Transit (derived)		
$a/R_\star$	$14.21^{+0.35}_{-0.27}$	$18.41^{+0.43}_{-0.59}$	$9.30^{+0.15}_{-0.22}$	$12.26^{+0.26}_{-0.27}$
i (deg)	$89.46^{+0.37}_{-0.48}$	$89.21^{+0.44}_{-0.37}$	$88.75^{+0.75}_{-0.65}$	87.01 ± 0.20
T_{14} (hr)	$2.130^{+0.077}_{-0.073}$	$2.581^{+0.017}_{-0.018}$	$1.918^{+0.016}_{-0.014}$	$1.232^{+0.038}_{-0.031}$
		Contaminant (derived)		
$\beta_g - \beta_{z_s}$	$-0.01^{+0.14}_{-0.10}$	-0.06 ± 0.07	$-0.09^{+0.06}_{-0.05}$	$-0.06^{+0.15}_{-0.14}$
$\beta_r - \beta_{z_s}$	$0.00^{+0.13}_{-0.07}$	$-0.05^{+0.06}_{-0.07}$	$-0.09^{+0.06}_{-0.05}$	-0.05 ± 0.13
$\beta_i - \beta_{z_s}$	$0.00^{+0.07}_{-0.02}$	$-0.02^{+0.03}_{-0.04}$	-0.04 ± 0.03	-0.02 ± 0.06
$\beta_{TESS} - \beta_{z_s}$	$0.23^{+0.18}_{-0.20}$	$0.30^{+0.09}_{-0.08}$	-0.13 ± 0.06	0.00 ± 0.17
$\beta_{\mathrm{QLP/HSLP}} - \beta_{z_s}$	–	–	–	$0.15^{+0.14}_{-0.12}$
$\beta_{\mathrm{CHEOPS}} - \beta_{z_s}$	–	$0.30^{+0.08}_{-0.07}$	–	–

Table 5. Final planetary parameters.

Parameter	TOI-2133 b	TOI-5734 b	TOI-5938 b	TOI-7009 b
		Transit (fitted)		
$R_p/R_\star$	0.03507 ± 0.00084	0.03569 ± 0.00059	0.04915 ± 0.00060	0.0603 ± 0.0016
P (d)	$3.8266472^{+5.0e-6}_{-4.0e-6}$	$6.1842161^{+5.3e-6}_{-6.1e-6}$	$2.2604240^{+3.6e-6}_{-3.3e-6}$	$2.3206612^{+4.2e-6}_{-4.4e-6}$
T_0 (BTJD)	$1985.8831^{+0.0013}_{-0.0016}$	$1848.6877^{+0.0017}_{-0.0015}$	2820.1815 ± 0.0010	3392.3627 ± 0.0005
$\rho_\star$ ($\rho_\odot$)	$2.61^{+0.21}_{-0.13}$	$2.22^{+0.14}_{-0.19}$	$2.13^{+0.10}_{-0.14}$	3.27 ± 0.20
b	$0.12^{+0.11}_{-0.09}$	$0.23^{+0.11}_{-0.13}$	$0.19^{+0.10}_{-0.12}$	$0.744^{+0.017}_{-0.018}$
		Transit (derived)		
$a/R_\star$	$14.17^{+0.38}_{-0.24}$	$18.49^{+0.37}_{-0.55}$	$9.32^{+0.21}_{-0.14}$	$10.95^{+0.22}_{-0.23}$
i (deg)	$89.50^{+0.35}_{-0.47}$	$89.29^{+0.42}_{-0.36}$	$88.85^{+0.72}_{-0.65}$	86.10 ± 0.16
T_{14} (hr)	$2.113^{+0.040}_{-0.061}$	$2.582^{+0.016}_{-0.017}$	1.915 ± 0.014	$1.227^{+0.022}_{-0.021}$
		Planetary and orbital		
R_p ($R_\oplus$)	2.37 ± 0.09	2.76 ± 0.09	3.82 ± 0.11	3.71 ± 0.15
M_p ($M_\oplus$)[a]	$8.3^{+3.4}_{-2.5}$	$9.7^{+4.7}_{-3.2}$	$15.6^{+8.0}_{-7.1}$	$14.8^{+7.4}_{-6.6}$
$K_\star$ ($m\,s^{-1}$)[a]	$4.6^{+1.9}_{-1.4}$	$4.1^{+2.0}_{-1.4}$	$9.3^{+4.7}_{-4.2}$	$10.2^{+5.1}_{-4.6}$
a (au)	0.0410 ± 0.0015	0.0607 ± 0.0023	0.0308 ± 0.0010	0.0287 ± 0.0010
$T_{p,eq}$ (K)	798 ± 12	788^{+14}_{-11}	1077^{+16}_{-15}	872^{+11}_{-10}
TSM	47^{+21}_{-14}	131^{+66}_{-43}	75^{+64}_{-26}	47^{+38}_{-16}
ESM	$6.02^{+0.36}_{-0.34}$	$13.22^{+0.86}_{-0.65}$	$15.57^{+0.67}_{-0.54}$	$9.20^{+0.60}_{-0.57}$

[a]Planetary masses and radial-velocity semi-amplitudes are estimated using theoretical mass–radius relations L. Zeng et al. (2019).

Downloaded from academic.oup.com/mnras/article/549/3/stag183/8442244 by UNIV LEIGE FAC PSYCH SCIENCES L'EDUCATION user on 26 November 2026

inferred planet-to-star radius ratio by approximately 6 per cent (2.4σ).

Similarly, for TOI-5734 b the model including free β_{TESS} and $\beta_{\rm CHEOPS}$ terms is strongly favoured over the contamination-free scenario (ΔAIC $= -78.4$), as well as over models including only β_{TESS} (ΔAIC $= -58.6$) or only $\beta_{\rm CHEOPS}$ (ΔAIC $= -36.9$). The corresponding dilution terms are $\beta_{TESS} = 0.34 \pm 0.05$ and $\beta_{\rm CHEOPS} = 0.35 \pm 0.04$. The contamination-free fit underestimates the radius ratio by approximately 10 per cent (5.7σ).

For TOI-5938 b, the model including a β_{TESS} term yields a marginally lower AIC than the contamination-free scenario (ΔAIC $= -1.1$), but this difference is not statistically significant. In fact, both models yield consistent radius ratios within a fraction of 1σ.

For TOI-7009 b, there is a moderate preference for including a $\beta_{\rm QLP/HSLP}$ term compared to a model with no contamination term (ΔAIC $= -2.7$), but no evidence supporting a β_{TESS} term from the SPOC PDCSAP data. The inferred dilution term is $\beta_{\rm QLP/HSLP} = 0.18 \pm 0.08$. The contamination-free fit underestimates the radius ratio by approximately 3 per cent (1.2σ), unless the QLP/HSLP data are ignored.

5.3 Additional tests

We performed a set of variant fits to assess the robustness of our results and their dependence on prior assumptions.

We tested replacing our Gaussian, spectroscopically informed stellar-density priors with uniform priors between 0 and 1000 $\rho_\odot$. The resulting stellar-density posteriors are skewed, with well-defined upper limits encompassing the spectroscopic density priors, and exhibit a broad degeneracy with the impact parameter. Overall, the inferred parameters remain consistent within 1σ of the fiducial solution, albeit with generally increased uncertainties. In particular, the error bars on the radius ratios are larger by factors of 2.0 for TOI-2133.01 and $\sim$1.3 for the others. The FPP (MC) values are largely unaffected, except for TOI-2133.01, which slightly decreases to $\sim$0.05, but still remains above the threshold for this criterion.

We also tested fits allowing for eccentric orbits, but the photometric data alone did not provide meaningful constraints.

6 DISCUSSION

6.1 *TESS* dilution and systematics

Owing to its 21 arcsec pixel scale, *TESS* SAP photometry is susceptible to flux contamination from unresolved nearby sources, to a much greater extent than *Kepler*. The PDC module of the SPOC pipeline applies a crowding correction term to account for contaminating flux within the aperture, but this correction relies on a modelled Point Response Function and catalogue information, which may be incomplete or inaccurate for faint or unresolved nearby sources.

The lack of PDC processing in the QLP/HSLP data sets may explain why a dilution term is detected for TOI-7009 in these data, whereas no such term is seen in the PDCSAP data for the same target. An imperfect PDC crowding correction may explain the dilution terms detected for TOI-2133 and TOI-5734, which, if neglected, would lead to an underestimation of the radius ratios by approximately 6 per cent and 10 per cent, respectively (see Section 5.2). These results are consistent with a recent study of the overall *TESS* population, which reported an average underestimation of 6 per cent for the radius ratio based on the official data products, with a large spread in the bias on a case-by-case basis (T. Han et al. 2025).

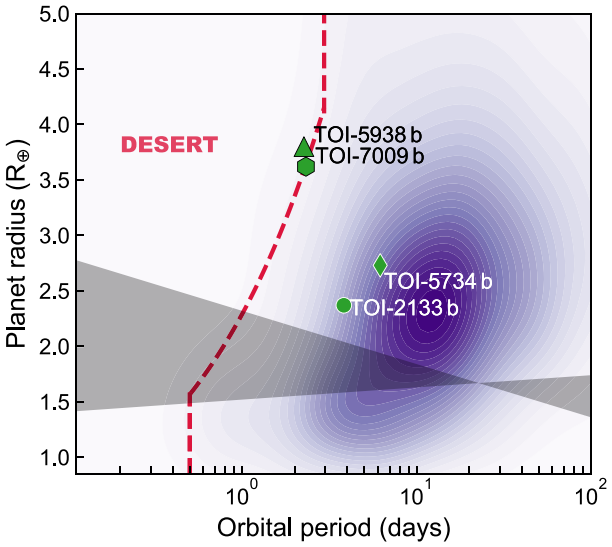


Figure 4. Location of the validated new planets TOI-2133 b (circle), TOI-5734 b (diamond), TOI-5938 b (triangle), and TOI-7009 b (hexagon). The different density levels and the corresponding colourmap indicate planet occurrence, with purpler regions being more populated and whiter regions less populated. The red dashed line marks the boundary of the Neptune desert, as defined by A. Castro-González et al. (2024). The black-shaded region shows the radius valley of sub-Neptune exoplanets around low mass stars measured by R. Cloutier & K. Menou (2020) and the radius valley for exoplanets around Sun-like stars measured by C. F. Martinez et al. (2019), scaled to low mass stars by R. Cloutier & K. Menou (2020).

6.2 Demographic context: radius valley and Neptune desert

Fig. 4 displays the validated planets and the candidate in the radius–orbital period diagram (see Table 5 for system parameters). All objects are located above the radius valley, suggesting that they should retain substantial gaseous envelopes. TOI-2133 b and TOI-5734 b lie close to the upper boundary of the radius valley, in a region where planets may either retain part of their primordial H_2–He envelopes or be water-rich with steam-dominated atmospheres. Instead, TOI-5938 b and TOI-7009 b lie at the edge of the Neptune desert, according to the revised, tighter boundaries reported by A. Castro-González et al. (2024). The latter two objects are rare within the known exoplanet population, occupying a sparsely populated region of parameter space that provides a unique window into the properties and evolution of close-in Neptune-sized planets.

6.3 Prospects for mass determination

To characterize planetary interiors and atmospheres, it is crucial first to accurately measure their masses, thereby breaking degeneracies in theoretical models (see, e.g. C. Dorn et al. 2015, 2017; M. Plotnykov & D. Valencia 2020; S. Bloot et al. 2023; L. Acuña et al. 2024; M. Plotnykov & D. Valencia 2024; C. Wilkinson et al. 2024). In this subsection, we estimate the radial velocity follow-up effort required to measure the masses of our four planets, assuming that the observational campaign is conducted using the MAROON-X spectrograph (A. Seifahrt et al. 2020), following K.

Downloaded from academic.oup.com/mnras/article/549/3/stag183/8442244 by UNIV LEIGE FAC PSYCH SCIENCES L'EDUCATION user on 26 November 2026

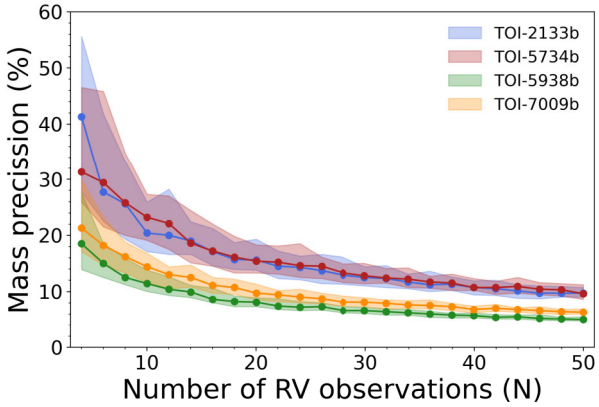


Figure 5. Expected mass precision as a function of the number of RV observations for TOI-2133 b, TOI-5734 b, TOI-5938 b, and TOI-7009 b. Solid lines indicate the median precision from our simulations, with shaded areas representing the 16th–84th percentiles.

Barkaoui et al. (2025a). To this end, we generated synthetic RV time series by randomly sampling observation dates within the allowed visibility window and evaluating the Keplerian signal of the known planets, based on the mass estimates reported in Table 5. We estimated the per-epoch uncertainty using an effective error ($\sigma_{\rm eff}$) computed directly using the publicly available exposure time calculator[9] that allows us to estimate the expected S/N for a given spectral type and magnitude and derive the Serval RV uncertainties for the blue and red arms. In addition to the internal RV uncertainties provided by the MAROON-X exposure time calculator, we include an additional RV jitter term to account for stellar and instrumental variability not captured by the formal per-epoch errors. Empirical studies based on large RV surveys have shown that photometrically quiet K dwarfs typically exhibit intrinsic RV variability at the level of a few $\mathrm{m\,s^{-1}}$, with a characteristic noise floor of $\sim$1.5–2.5 $\mathrm{m\,s^{-1}}$ for inactive stars (e.g. J. T. Wright 2005; H. Isaacson & D. Fischer 2010). Following these results, we adopt a conservative fixed jitter of $2\,\mathrm{m\,s^{-1}}$, which is added in quadrature to the internal MAROON-X uncertainties to define the effective per-epoch error used in our simulations.

Then, we use N to refer to the number of RV measurements in an observing campaign. For each set of N observations, we calculated the noiseless Keplerian RVs induced by the planets and created 100 Monte Carlo simulations by adding Gaussian noise with a standard deviation of $\sigma_{\rm eff}$. It is important to note that, for simplicity, this approach treats the additional RV jitter as an uncorrelated noise term and does not explicitly model time-correlated stellar activity signals or multiparameter correlations. In the next step, each set of N simulated observations was fitted using the `curve_fit` function from the SCIPY library (P. Virtanen et al. 2020), treating planetary mass as a free parameter. Although this method is less sophisticated than a full multiparameter Bayesian analysis, it provides a practical way to assess how mass uncertainty scales with N and to approximate the observational effort required to reach a given precision.

The results of using this methodology are shown in Fig. 5. On the one hand, we found that for TOI-7009 b and TOI-5938 b we can reach mass precisions of $\sim$10 per cent with $\sim$30 observations. On the other hand, for TOI-2133 b and TOI-5734 b we can reach about $\sim$15 per cent of mass precision with $\sim$50 observations. In all cases, since the observational windows for these planets are approximately five months long, a moderate observational campaign spanning one semester can provide accurate planetary masses for all of them, enabling future efforts to model their internal structures and atmospheric properties.

[9] https://maroon-x-etc.gemini.edu/app

6.4 Prospects for atmospheric characterization

To gauge the prospects for atmospheric characterization of our newly validated planets, we computed the Transmission Spectroscopy Metric (TSM) and Emission Spectroscopy Metric (ESM) following E. M. R. Kempton et al. (2018). TOI-5734 b and TOI-5938 b have TSM values near or above the recommended threshold of 80, classifying them among the most promising targets for atmospheric follow-up, despite significant uncertainties due to the use of empirical mass estimates. TOI-2133 b and TOI-7009 b remain within the feasible range for atmospheric characterization with just one or a few *James Webb Space Telescope* (*JWST*) visits, with TSM values comparable to K2-18 b. Although the ESM scale was not formally calibrated for sub-Neptunes, our targets fall in the upper half of planets of similar size with radius precision better than 4 per cent, highlighting their suitability for emission spectroscopy studies. To gauge the prospects for atmospheric characterization of our newly validated planets, we computed the Transmission Spectroscopy Metric (TSM) and Emission Spectroscopy Metric (ESM) following E. M. R. Kempton et al. (2018) (see Table 5 and Fig. 6).

We further investigated the potential of *JWST* observations of to probe the atmosphere of TOI-5938 b, our newly validated resident of the Neptune desert with the highest ESM and second-highest TSM in our sample. We used `TauREx 3` (I. P. Waldmann et al. 2015a, b; A. F. Al-Refaie et al. 2021) to synthesize transmission and emission spectra for various atmospheric scenarios: H_2–He envelopes with 1× and 100× solar metallicity including haze (analogous to previous simulations, e.g. J. Orell-Miquel et al. 2023; E. Goffo et al. 2024); two compositions motivated by retrievals of TOI-421 b (B. Davenport et al. 2025), a mini-Neptune with a comparable equilibrium temperature; and a pure steam H_2O atmosphere. The temperature–pressure profiles were adapted from a grid published by P. Mollière et al. (2015).

Spectral error bars for *JWST* NIRISS SOSS (0.6–2.8 μm), NIRSpec G395H (2.88–5.20 μm), and MIRI LRS (5–12 μm) instrumental modes were computed with `ExoTETHyS` (G. Morello et al. 2021), including a conservative 30 per cent safety margin. Our simulations show that a single transit observation is sufficient to capture the main molecular features, except in the case of a steam or otherwise heavy atmosphere (see Fig. 7). The thermal emission is readily detectable at mid-infrared wavelengths, but multiple visits are likely required to constrain its spectral slope and features, enabling discrimination between different atmospheric scenarios.

6.5 Search for additional transiting planets in the *TESS* photometry

We employed the `SHERLOCK` package (F. J. Pozuelos et al. 2020) to explore the publicly available *TESS* data for each TOI analysed in this study. Our goal was to recover the officially alerted candidates independently and to search for hints of potential candidates that may have been overlooked by the SPOC and QLP pipelines (see, e.g. G. Dransfield et al. 2024; S. Yalçinkaya et al.

Downloaded from academic.oup.com/mnras/article/549/3/stag183/8442244 by UNIV LEIGE FAC PSYCH SCIENCES L'EDUCATION user on 26 November 2026

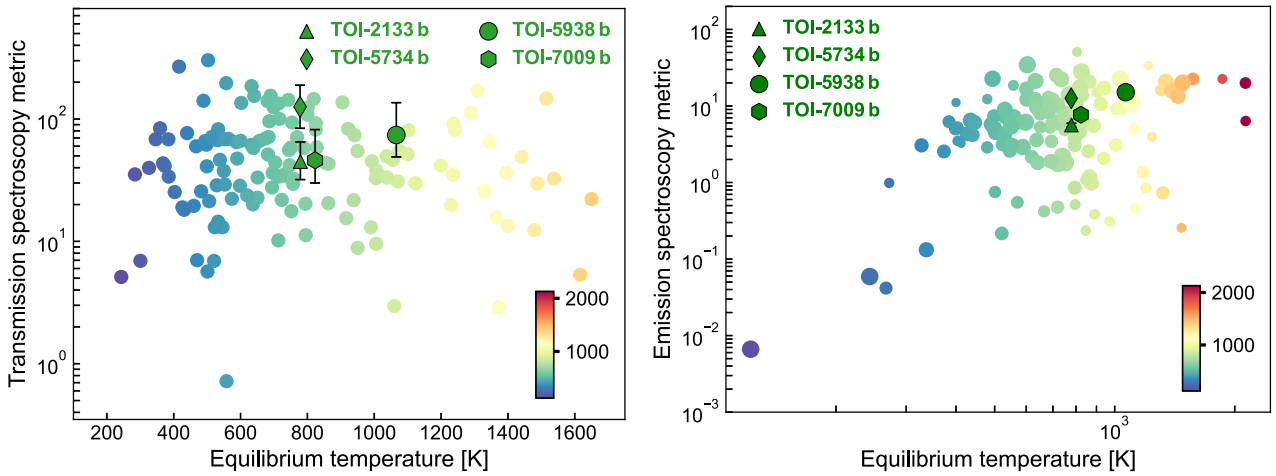


Figure 6. Transmission spectroscopy metric (left) and emission spectroscopy metric (right) as a function of equilibrium temperature for confirmed transiting sub-Neptune exoplanets, along with TOI-2133 b (circle), TOI-5734 b (diamond), TOI-5938 b (triangle), and TOI-7009 b (hexagon). For the ESM panel, only planets with radius uncertainties below 4 per cent are included. Data were extracted from `NASA Exoplanet Archive`.

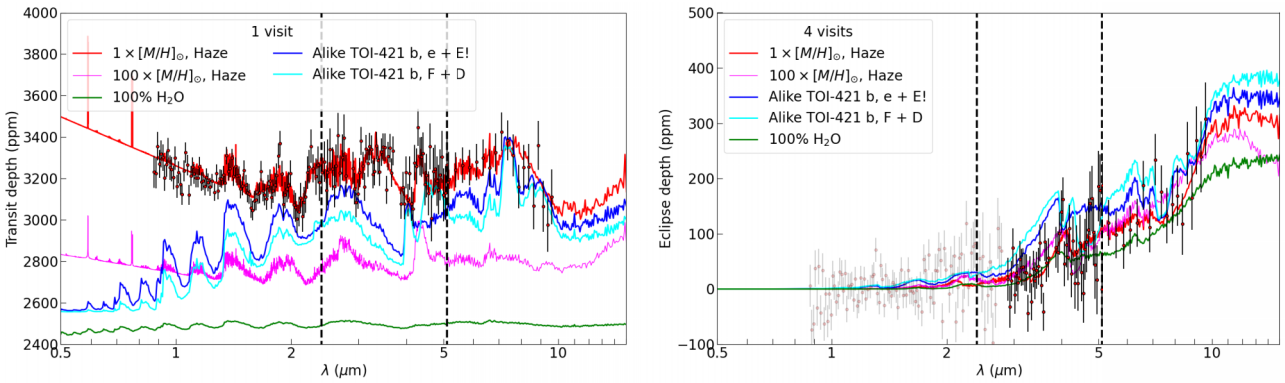


Figure 7. Modelled transmission (left) and emission (right) spectra of TOI-5938 b are shown under different atmospheric assumptions: an H_2–He envelope with 1–100× solar abundances and haze, a TOI-421 b-like composition (mini-Neptune of similar temperature; B. Davenport et al. 2025), or a steam H_2O atmosphere. Simulated *JWST* spectra with NIRISS SOSS, NIRSpec G395H, and MIRI LRS are overplotted, assuming one transit (left) or four eclipses (right).

2025; S. Zúñiga-Fernández et al. 2025). We refer the reader to F. J. Pozuelos et al. (2023) for further details on different search strategies. For the most up-to-date version of the pipeline and a full description of its functionalities, see M. Dévora-Pajares et al. (2024). To this end, we combined all available 120 s cadence sectors for each TOI; for TOI-7009, we additionally included the available 200 s cadence sectors. We then explored orbital periods between 0.5 and 20 d in all cases. This choice was motivated by computational feasibility and the assumption that planets with longer periods would likely not transit under a co-planar system (see, e.g. J. S. Jenkins et al. 2019). In all cases, we successfully recovered the alerted candidates. This allowed us to confirm these alerts independently. However, aside from these candidates, we did not identify any additional signals that could be considered hints of planetary candidates.

7 CONCLUSIONS

We have presented the validation of four new transiting planets discovered by *TESS* around K-dwarf stars. Our analysis combined multicolour photometry, statistical validation, and a novel neural-network classifier, producing a largely consistent picture while revealing some method-dependent differences. Multicolour photometry provides the strongest validation in three of the four cases, owing to its higher information content, but its effectiveness is limited for small planets and by data quality, as also noted by A. Peláez-Torres et al. (2024). WATSON-Net is confirmed as an efficient alternative to Bayesian validation tools, delivering similar performance at lower computational cost.

These systems are valuable benchmarks for comparative exoplanetology. Their K-dwarf hosts provide an advantageous regime for precise mass measurements and atmospheric studies, being more accessible than FG systems while less impacted by stellar activity than M dwarfs. In particular, TOI-5938 b and TOI-7009 b emerge as a rare residents of the Neptune desert, with favourable transmission and emission spectroscopy metrics that make them high-priority targets for *JWST*.

Expanding the sample of well-characterized K-dwarf sub-Neptunes will enable rigorous tests of formation and evolution processes, including photoevaporation and core-powered mass loss, and help clarify the origins of the radius valley and Neptune desert boundaries.

Downloaded from academic.oup.com/mnras/article/549/3/stag183/8442244 by UNIV LEIGE FAC PSYCH SCIENCES L'EDUCATION user on 26 November 2026

ACKNOWLEDGEMENTS

GM acknowledges financial support from the Severo Ochoa grant CEX2021-001131-S and from the Ramón y Cajal grant RYC2022-037854-I funded by MCIN/AEI/1144 10.13039/501100011033 and FSE+. FM acknowledges financial support from the Agencia Estatal de Investigación del Ministerio de Ciencia, Innovación y Universidades (MCIU/AEI) through grant PID2023-152906NA-I00. BR-A acknowledges funding support from the ANID Basal project FB210003. Funding for KB was provided by the European Union (ERC AdG SUBSTELLAR, GA 101054354). BVR acknowledges support from the National Aeronautics and Space Administration under agreement no. 80NSSC21K0593 for the programme 'Alien Earths', and the European Research Council (ERC) Synergy Grant under the European Union's Horizon 2020 research and innovation programme (grant no. 101118581 – project REVEAL). The results reported herein benefited from collaborations and/or information exchange within NASA's Nexus for Exoplanet System Science (NExSS) research coordination network sponsored by NASA's Science Mission Directorate. EE-B acknowledges financial support from the European Union and the State Agency of Investigation of the Spanish Ministry of Science and Innovation (MICINN) under the grant PRE2020-093107 of the Pre-Doc Programme for the Training of Doctors (FPI-SO) through FSE funds. The authors acknowledge support from the Swiss NCCR PlanetS and the Swiss National Science Foundation. This work has been carried out within the framework of the NCCR PlanetS supported by the Swiss National Science Foundation under grants 51NF40182901 and 51NF40205606. JK acknowledges support from the Swiss National Science Foundation under grant number TMSGI2_211697. MG is FNRS Research Director. He thanks the Wallonian Region and the University of Liege for their contribution to the funding of, respectively, the SPECULOOS-North/Artemis and SAINT-EX telescopes.This article is based on observations made with the MuSCAT2 instrument, developed by ABC, at TCS operated on the island of Tenerife by the IAC in the Spanish Observatorio del Teide. This work is partly supported by JSPS KAKENHI grant numbers JP18H01265 and JP18H05439, and JST PRESTO grant number JPMJPR1775. We acknowledge financial support from the Agencia Estatal de Investigación of the Ministerio de Ciencia e Innovación MCIN/AEI/10.13039/501100011033 and the ERDF 'A way of making Europe' through project PID2021-125627OB-C32, and from the Centre of Excellence 'Severo Ochoa' award to the Instituto de Astrofisica de Canarias. This work is partly supported by JSPS KAKENHI grant numbers JP24H00017, JP24K00689, JP21K13955, JP25K17450, JP24K17082, JP24H00248, JP24K17083, JSPS Grant-in-Aid for JSPS Fellows grant numbers JP24KJ0241, JP25KJ0091, JSPS Bilateral Programme Number JPJSBP120249910, JST SPRING, grant number JPMJSP2108 and JSPS Grant-in-Aid for JSPS Fellows grant number JP25KJ1036. The Joan Oró Telescope (TJO) of the Montsec Observatory (OdM) is owned by the Catalan Government and operated by the Institute for Space Studies of Catalonia (IEEC). Visiting Astronomer at the Infrared Telescope Facility, which is operated by the University of Hawaii under contract 80HQTR24DA010 with the National Aeronautics and Space Administration. This work makes use of observations from the LCOGT network. Part of the LCOGT telescope time was granted by NOIRLab through the Mid-Scale Innovations Programme (MSIP). MSIP is funded by NSF. In this study, the observational data obtained within the scope of project numbered 25ATUG100-3012 carried out using the TUG100 telescope at the TUG (TÜBİTAK National Observatory, Antalya) site of the Türkiye National Observatories have been utilized, and we express our gratitude for the invaluable support provided by the Türkiye National Observatories, the observation team, and all its staff. Some of the observations presented in this paper were carried out at the Observatorio Astronómico Nacional on the Sierra de San Pedro Mártir (OAN-SPM), Baja California, México. We acknowledge support from the Swiss National Science Foundation SPIRIT-216537. We acknowledge support from the Centre for Space and Habitability (CSH) of the University of Bern. Part of this work received support from the National Centre for Competence in Research PlanetS, supported by the Swiss National Science Foundation (SNSF). YGMC, AK, IPF, and MPM are partially supported by UNAM PAPIIT-IG101224. BOD acknowledges support from the Swiss State Secretariat for Education, Research and Innovation (SERI) under contract number MB22.00046. The work of HPO has been carried out within the framework of the NCCR PlanetS supported by the Swiss National Science Foundation under grants 51NF40_182901 and 51NF40_205606. YAl acknowledges support from the Swiss National Science Foundation (SNSF) under grant 200020_192038. TWi acknowledges support from the UKSA and the University of Warwick. AD acknowledges financial support from the Swiss National Science Foundation (SNSF) for project 200021_200726. PM acknowledges support from STFC research grant number ST/R000638/1. MNG is the ESA CHEOPS Project Scientist and Mission Representative and is responsible for the Guest Observers (GO) Programme but does not relay proprietary information between the GO and Guaranteed Time Observation (GTO) Programmes, nor decide on the definition and target selection of the GTO Programme. This research has made use of the Exoplanet Follow-up Observation Programme (ExoFOP; DOI: 10.26134/ExoFOP5) website, which is operated by the California Institute of Technology, under contract with the National Aeronautics and Space Administration under the Exoplanet Exploration Programme. Funding for the *TESS* mission is provided by NASA's Science Mission Directorate. KAC acknowledges support from the *TESS* mission via subaward s3449 from MIT. Support by the Spanish Ministry of Science and Innovation with the Ramon y Cajal fellowship number RYC2021-031798-I, and funding from the University of La Laguna.

DATA AVAILABILITY

TESS data used in this work are publicly available from the MAST at https://archive.stsci.edu/. Some of the ground-based photometric and spectroscopic data obtained through the TFOP are publicly available or will be made available upon reasonable request to the corresponding author.

REFERENCES

Acuña L., Kreidberg L., Zhai M., Mollière P., 2024, A&A, 688, A60
Akaike H., 1974, IEEE Trans. Autom. Control, 19, 716
Al-Refaie A. F., Changeat Q., Waldmann I. P., Tinetti G., 2021, ApJ, 917, 37
Aller A., Lillo-Box J., Jones D., Miranda L. F., Barceló Forteza S., 2020, A&A, 635, A128
Barkaoui K. et al., 2023, A&A, 677, A38
Barkaoui K. et al., 2024, A&A, 687, A264
Barkaoui K. et al., 2025a, MNRAS, 544, 2637
Barkaoui K. et al., 2025b, A&A, 696, A44
Benz W. et al., 2021, Exp. Astron., 51, 109

Downloaded from academic.oup.com/mnras/article/549/3/stag183/8442244 by UNIV LEIGE FAC PSYCH SCIENCES L'EDUCATION user on 26 November 2026

Berger T. A., Huber D., Gaidos E., van Saders J. L., Weiss L. M., 2020, AJ, 160, 108
Biagini A., Cracchiolo G., Petralia A., Maldonado J., Di Maio C., Micela G., 2024, MNRAS, 530, 1054
Bieryla A. et al., 2021, Stellar Parameter Classification of TESS recon spectra from TRES and FIES, version v1, Zenodo
Bieryla A., Latham D., Quinn S., Collins K., Esquerdo G., Calkins M., Berlind P., Mink J., 2023, American Astronomical Society Meeting Abstracts. p. 267.08
Bitsch B., Raymond S. N., Izidoro A., 2019, A&A, 624, A109
Bloot S., Miguel Y., Bazot M., Howard S., 2023, MNRAS, 523, 6282
Brahm R., Jordán A., Hartman J., Bakos G., 2017, MNRAS, 467, 971
Brown T. M. et al., 2013, PASP, 125, 1031
Buchhave L. A. et al., 2010, ApJ, 720, 1118
Buchhave L. A. et al., 2012, Nature, 486, 375
Burdanov A. Y. et al., 2022, PASP, 134, 105001
Burgasser A. J., Splat Development Team, 2017, Astron. Soc. India Conf. Ser. Vol. 4, The SpeX Prism Library Analysis Toolkit (SPLAT): A Data Curation Model, p. 7
Burrows A., Hubbard W. B., Lunine J. I., Liebert J., 2001, Rev. Mod. Phys., 73, 719
Castelli F., Kurucz R. L., 2003, in Piskunov N., Weiss W. W., Gray D. F., eds, Proc. IAU Symp. 210, Modelling of Stellar Atmospheres. Kluwer, Dordrecht, p. A20
Castro-González A., Bourrier V., Lillo-Box J., Delisle J. B., Armstrong D. J., Barrado D., Correia A. C. M., 2024, A&A, 689, A250
Cevallos Soto A., Tan J. C., Hu X., Hsu C.-J., Walsh C., 2022, MNRAS, 517, 2285
Chatterjee S., Tan J. C., 2014, ApJ, 780, 53
Chiang E., Laughlin G., 2013, MNRAS, 431, 3444
Claret A., 2018, A&A, 618, A20
Cloutier R., Menou K., 2020, AJ, 159, 211
Collins K., 2019, American Astronomical Society Meeting Abstracts #233. p. 140.05
Collins K. A., Kielkopf J. F., Stassun K. G., Hessman F. V., 2017, AJ, 153, 77
Colome J., Ribas I., 2006, IAU Special Session. p. 11
Colomé J., Francisco X., Ribas I., Casteels K., Martín J., 2010, in Radziwill N. M., Bridger A., eds, Proc. SPIE Conf. Ser. Vol. 7740, Software and Cyberinfrastructure for Astronomy. SPIE, Bellingham, p. 774009
Cushing M. C., Vacca W. D., Rayner J. T., 2004, PASP, 116, 362
Cushing M. C., Rayner J. T., Vacca W. D., 2005, ApJ, 623, 1115
Davenport B. et al., 2025, ApJ, 984, L44
Dekany R. et al., 2013, ApJ, 776, 130
Delrez L. et al., 2022, A&A, 667, A59
Demory B. O. et al., 2020, A&A, 642, A49
Dévora-Pajares M., Pozuelos F. J., Thuillier A., Timmermans M., Van Grootel V., Bonidie V., Mota L. C., Suárez J. C., 2024, MNRAS, 532, 4752
Dévora-Pajares M., Pozuelos F. J., Suárez J. C., González-Penedo M., Dafonte C., 2025, preprint (arXiv:2511.08768)
Dorn C., Khan A., Heng K., Connolly J. A. D., Alibert Y., Benz W., Tackley P., 2015, A&A, 577, A83
Dorn C., Venturini J., Khan A., Heng K., Alibert Y., Helled R., Rivoldini A., Benz W., 2017, A&A, 597, A37
Dransfield G. et al., 2024, MNRAS, 527, 35
Egger J. A. et al., 2024, A&A, 688, A223
Fűrész G., 2008, PhD thesis, Univ. Szeged, Hungary
Foreman-Mackey D., Agol E., Ambikasaran S., Angus R., 2017, AJ, 154, 220
Fulton B. J., Petigura E. A., 2018, AJ, 156, 264
Fulton B. J. et al., 2017, AJ, 154, 109
Furlan E. et al., 2017, AJ, 153, 71
Garcia L. J., Timmermans M., Pozuelos F. J., Ducrot E., Gillon M., Delrez L., Wells R. D., Jehin E., 2022, MNRAS, 509, 4817
Ghachoui M. et al., 2023, A&A, 677, A31
Ghachoui M. et al., 2024, A&A, 690, A263
Giacalone S. et al., 2021, AJ, 161, 24
Giacalone S. et al., 2022, AJ, 163, 99
Gillon M. et al., 2024, Nat. Astron., 8, 865
Ginzburg S., Schlichting H. E., Sari R., 2018, MNRAS, 476, 759
Goffo E. et al., 2024, A&A, 685, A147
Gupta A., Schlichting H. E., 2019, MNRAS, 487, 24
Gupta A., Schlichting H. E., 2020, MNRAS, 493, 792
Han T., Robertson P., Brandt T. D., Kanodia S., Cañas C., Shporer A., Ricker G., Beard C., 2025, ApJ, 988, L4
Hayward T. L., Brandl B., Pirger B., Blacken C., Gull G. E., Schoenwald J., Houck J. R., 2001, PASP, 113, 105
Heng K., Owen J. E., Tian M., 2025, ApJ, 994, 28
Hestroffer D., 1997, A&A, 327, 199
Howell S. B., Everett M. E., Sherry W., Horch E., Ciardi D. R., 2011, AJ, 142, 19
Hsu D. C., Ford E. B., Ragozzine D., Ashby K., 2019, AJ, 158, 109
Huang C. X. et al., 2020, Res. Notes Am. Astron. Soc., 4, 204
Husser T. O., Wende-von Berg S., Dreizler S., Homeier D., Reiners A., Barman T., Hauschildt P. H., 2013, A&A, 553, A6
Inamdar N. K., Schlichting H. E., 2015, MNRAS, 448, 1751
Isaacson H., Fischer D., 2010, ApJ, 725, 875
Izidoro A., Bitsch B., Raymond S. N., Johansen A., Morbidelli A., Lambrechts M., Jacobson S. A., 2021a, A&A, 650, A152
Izidoro A., Bitsch B., Dasgupta R., 2021b, ApJ, 915, 62
Jehin E. et al., 2018, The Messenger, 174, 2
Jenkins J. M. et al., 2016, in Chiozzi G., Guzman J. C., eds, Proc. SPIE Conf. Ser. Vol. 9913, Software and Cyberinfrastructure for Astronomy IV. SPIE, Bellingham, p. 99133E
Jenkins J. S., Pozuelos F. J., Tuomi M., Berdiñas Z. M., Díaz M. R., Vines J. I., Suárez J. C., Peña Rojas P. A., 2019, MNRAS, 490, 5585
Jordan D., Song I., 2025, AJ, 169, 234
Kempton E. M. R. et al., 2018, PASP, 130, 114401
Kipping D. M., 2010, MNRAS, 408, 1758
Kite E. S., Fegley B., Jr, Schaefer L., Ford E. B., 2019, ApJ, 887, L33
Kunimoto M., Bryson S., 2021, AJ, 161, 69
Kunimoto M., Matthews J. M., 2020, AJ, 159, 248
Kurucz R. L., 1992, in Barbuy B., Renzini A., eds, Proc. IAU Symp. 149, The Stellar Populations of Galaxies. Kluwer, Dordrecht, p. 225
Lang D., Hogg D. W., Mierle K., Blanton M., Roweis S., 2010, AJ, 139, 1782
Lillo-Box J. et al., 2022, A&A, 667, A102
Liu B., Ormel C. W., Lin D. N. C., 2017, A&A, 601, A15
Lucy L. B., Sweeney M. A., 1971, AJ, 76, 544
Luque R., Pallé E., 2022, Science, 377, 1211
Mann A. W., Brewer J. M., Gaidos E., Lépine S., Hilton E. J., 2013, AJ, 145, 52
Martinez C. F., Cunha K., Ghezzi L., Smith V. V., 2019, ApJ, 875, 29
Mazeh T., Holczer T., Faigler S., 2016, A&A, 589, A75
McCully C., Volgenau N. H., Harbeck D.-R., Lister T. A., Saunders E. S., Turner M. L., Siiverd R. J., Bowman M., 2018, in Guzman J. C., Ibsen J., eds, Proc. SPIE Conf. Ser. Vol. 10707, Software and Cyberinfrastructure for Astronomy V. SPIE, Bellingham, p. 107070K
Mollière P., van Boekel R., Dullemond C., Henning T., Mordasini C., 2015, ApJ, 813, 47
Morello G., Tsiaras A., Howarth I. D., Homeier D., 2017, AJ, 154, 111
Morello G., Claret A., Martin-Lagarde M., Cossou C., Tsiara A., Lagage P.-O., 2020a, J. Open Source Softw., 5, 1834
Morello G., Claret A., Martin-Lagarde M., Cossou C., Tsiaras A., Lagage P. O., 2020b, AJ, 159, 75
Morello G., Zingales T., Martin-Lagarde M., Gastaud R., Lagage P.-O., 2021, AJ, 161, 174
Morello G., Dyrek A., Changeat Q., 2022, MNRAS, 517, 2151
Morello G. et al., 2023, A&A, 673, A32
Morris R. L., Twicken J. D., Smith J. C., Clarke B. D., Jenkins J. M., Bryson S. T., Girouard F., Klaus T. C., 2020, in Jenkins Jon M., ed., Kepler Data Processing Handbook: Photometric Analysis, Kepler Science Document KSCI-19081-003, id. 6
Morton T. D., 2015, Astrophysics Source Code Library, record ascl:1503.010
Narita N. et al., 2019, J. Astron. Telesc. Instrum. Syst., 5, 015001

Downloaded from academic.oup.com/mnras/article/549/3/stag183/8442244 by UNIV LEIGE FAC PSYCH SCIENCES L'EDUCATION user on 26 November 2026

Ogihara M., Kunitomo M., Hori Y., 2020, ApJ, 899, 91
Orell-Miquel J. et al., 2023, A&A, 669, A40
Owen J. E., Lai D., 2018, MNRAS, 479, 5012
Owen J. E., Wu Y., 2013, ApJ, 775, 105
Owen J. E., Wu Y., 2017, ApJ, 847, 29
Parviainen H. et al., 2019, A&A, 630, A89
Parviainen H. et al., 2020, A&A, 633, A28
Parviainen H., Luque R., Palle E., 2024, MNRAS, 527, 5693
Peláez-Torres A. et al., 2024, A&A, 690, A62
Plotnykov M., Valencia D., 2020, MNRAS, 499, 932
Plotnykov M., Valencia D., 2024, MNRAS, 530, 3488
Pozuelos F. J. et al., 2020, A&A, 641, A23
Pozuelos F. J. et al., 2023, A&A, 672, A70
Rackham B. V., Apai D., Giampapa M. S., 2018, ApJ, 853, 122
Rackham B. V., Apai D., Giampapa M. S., 2019, AJ, 157, 96
Rayner J. T., Toomey D. W., Onaka P. M., Denault A. J., Stahlberger W. E., Vacca W. D., Cushing M. C., Wang S., 2003, PASP, 115, 362
Rayner J. T., Cushing M. C., Vacca W. D., 2009, ApJS, 185, 289
Ricker G. R. et al., 2015, J. Astron. Telesc. Instrum. Syst., 1, 014003
Rogers J. G., Gupta A., Owen J. E., Schlichting H. E., 2021, MNRAS, 508, 5886
Rojas-Ayala B., Covey K. R., Muirhead P. S., Lloyd J. P., 2012, ApJ, 748, 93
Scott N. J., Howell S. B., Horch E. P., Everett M. E., 2018, PASP, 130, 054502
Sebastian D. et al., 2021, A&A, 645, A100
Seifahrt A. et al., 2020, in Evans C. J., Bryant J. J., Motohara K., eds, Proc. SPIE Conf. Ser. Vol. 11447, Ground-based and Airborne Instrumentation for Astronomy VIII. SPIE, Bellingham, p. 114471F
Smith J. C. et al., 2012, PASP, 124, 1000
Southworth J. et al., 2009, MNRAS, 396, 1023
Strakhov I. A., Safonov B. S., Cheryasov D. V., 2023, Astrophys. Bull., 78, 234
Stumpe M. C., Smith J. C., Catanzarite J. H., Van Cleve J. E., Jenkins J. M., Twicken J. D., Girouard F. R., 2014, PASP, 126, 100
Timmermans M. et al., 2024, A&A, 687, A48
Triaud A. H. M. J. et al., 2023, MNRAS, 525, L98
Tsiaras A., Waldmann I. P., Rocchetto M., Varley R., Morello G., Damiano M., Tinetti G., 2016, ApJ, 832, 202
Van Eylen V., Agentoft C., Lundkvist M. S., Kjeldsen H., Owen J. E., Fulton B. J., Petigura E., Snellen I., 2018, MNRAS, 479, 4786
Virtanen P. et al., 2020, Nat. Methods, 17, 261
Waldmann I. P., Tinetti G., Rocchetto M., Barton E. J., Yurchenko S. N., Tennyson J., 2015a, ApJ, 802, 107
Waldmann I. P., Rocchetto M., Tinetti G., Barton E. J., Yurchenko S. N., Tennyson J., 2015b, ApJ, 813, 13
Wilkinson C., Charnay B., Mazevet S., Lagrange A. M., Chomez A., Squicciarini V., Panek E., Mazoyer J., 2024, A&A, 692, A113
Winn J. N., Stefánsson G., 2025, Planet. Sci. J., 6, 300
Wright J. T., 2005, PASP, 117, 657
Yalçinkaya S. et al., 2025, A&A, 702, A209
Zeng L. et al., 2019, Proc. Natl. Acad. Sci., 116, 9723
Zúñiga-Fernández S. et al., 2025, A&A, 702, A85

APPENDIX A: HIGH-RESOLUTION IMAGES

Figs A1–A3 present the high-resolution images of the targets acquired as part of the TFOP, along with the corresponding contrast curves.

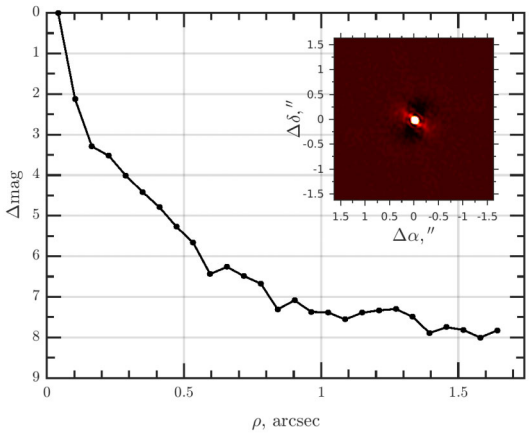


Figure A1. High-resolution imaging of TOI-5938 (I) obtained with the speckle polarimeter installed at the 2.5 m SAI telescope, together with the corresponding contrast curve as a function of angular separation. No stellar companions were detected within the sensitivity limits.

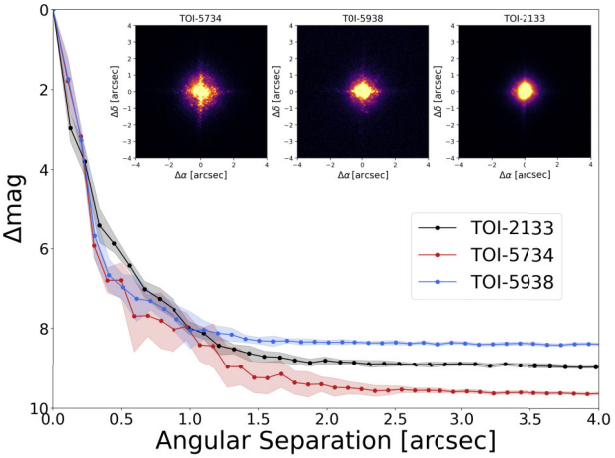


Figure A2. High-resolution imaging of TOI-2133 (Br-γ), TOI-5734 (K_c), and TOI-5938 (Br-γ) obtained with the PHARO instrument installed at the 5 m Hale telescope at Palomar Observatory, together with the corresponding contrast curves as a function of angular separation. No stellar companions were detected within the sensitivity limits for any of the targets.

Downloaded from academic.oup.com/mnras/article/549/3/stag183/8442244 by UNIV LEIGE FAC PSYCH SCIENCES L'EDUCATION user on 26 November 2026

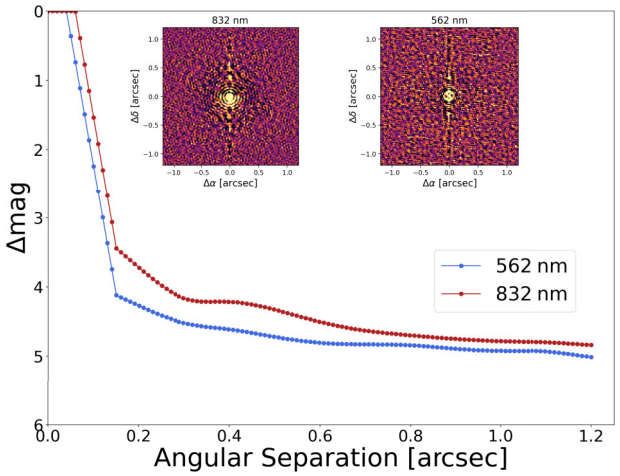


Figure A3. High-resolution imaging of TOI-7009 (562 and 832 nm) obtained with the NESSI speckle imager installed at the 3.5 m WYIN telescope, together with the corresponding contrast curves as a function of angular separation. No stellar companions were detected within the sensitivity limits.

APPENDIX B: ADDITONAL TPF IMAGES

Because the *TESS* target apertures differ slightly between sectors, Fig. B1 shows the TPF images for sectors not otherwise displayed.

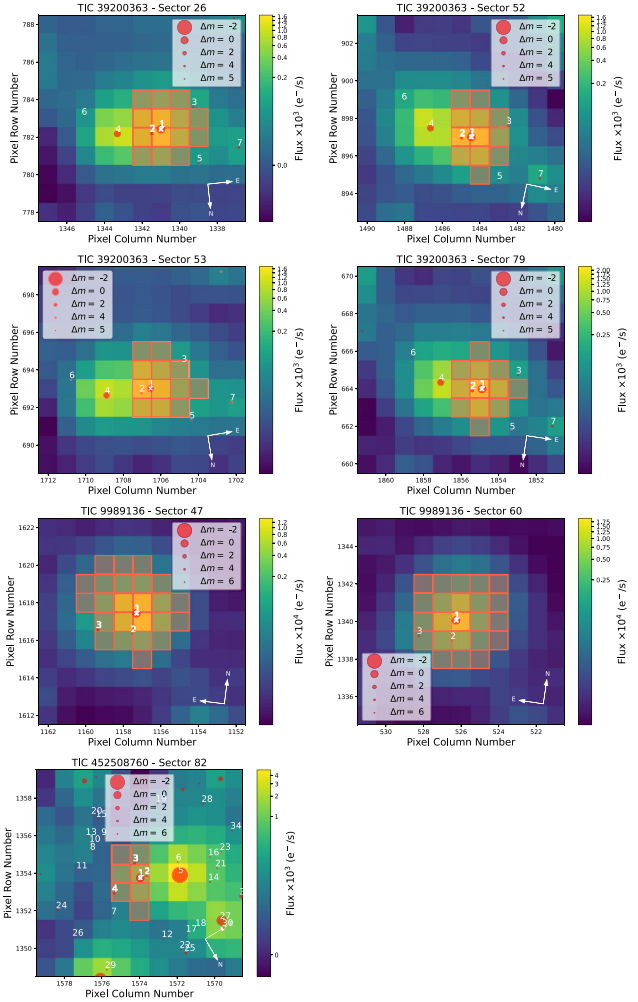


Figure B1. *TESS* TPF images from additional sectors (cf. Fig. 1).

APPENDIX C: MULTICOLOUR PHOTOMETRY: ADDITIONAL INFORMATION

Table C1 reports the parameter priors adopted in the multicolour photometry fits.

Figs C1 and C2 show the detrended transit light-curves that were included in the multicolour photometry analysis, beyond the *TESS* time series.

Figs C3–C6 show the full cornerplots from the light curve fittings for the multicolour photometry (Section 4.1). All cornerplots present typical parameter correlations, but the only critical case is that of TOI-2133 b (see Section 5 and Fig. C3).

Downloaded from academic.oup.com/mnras/article/549/3/stag183/8442244 by UNIV LEIGE FAC PSYCH SCIENCES L'EDUCATION user on 26 November 2026

Table C1. Prior probability distributions of the fitted parameters.

Parameter	TOI-2133.01	TOI-5734.01	TOI-5938.01	TOI-7009.01
		Transit		
$R_p/R_\star$	$\mathcal{U}(0, 1)$	$\mathcal{U}(0, 1)$	$\mathcal{U}(0, 1)$	$\mathcal{U}(0, 1)$
P (d)[a]	$\mathcal{N}(3.826659, 0.000048)$	$\mathcal{N}(6.184169, 0.000029)$	$\mathcal{N}(2.260431, 0.000039)$	$\mathcal{N}(2.320667, 0.000014)$
T_0 (BTJD)[a]	$\mathcal{N}(1985.8828, 0.0037)$	$\mathcal{N}(1848.6851, 0.0050)$	$\mathcal{N}(2820.1832, 0.0059)$	$\mathcal{N}(3392.3643, 0.0053)$
$\rho_\star$ ($\rho_\odot$)	$\mathcal{N}(2.70, 0.20)$	$\mathcal{N}(2.06, 0.19)$	$\mathcal{N}(2.06, 0.15)$	$\mathcal{N}(3.24, 0.21)$
b	$\mathcal{U}(0, 1 + p)$	$\mathcal{U}(0, 1 + p)$	$\mathcal{U}(0, 1 + p)$	$\mathcal{U}(0, 1 + p)$
		Contamination		
$T_{\star,\mathrm{eff}}$ (K)	4250	4790	4650	4080
$\log g_\star$ (dex)	4.60	4.59	4.59	4.63
$T_{c,\mathrm{eff}}$ (K)	$\mathcal{U}(2300, 12000)$	$\mathcal{U}(2300, 12000)$	$\mathcal{U}(2300, 12000)$	$\mathcal{U}(2300, 12000)$
$\log g_c$ (dex)	$\mathcal{U}(2.0, 5.5)$	$\mathcal{U}(2.0, 5.5)$	$\mathcal{U}(2.0, 5.5)$	$\mathcal{U}(2.0, 5.5)$
f_c[b]	$\mathcal{U}(-1000, 1000)$	$\mathcal{U}(-1000, 1000)$	$\mathcal{U}(-1000, 1000)$	$\mathcal{U}(-1000, 1000)$
β_{TESS}[b]	$\mathcal{U}(-1, 1)$	$\mathcal{U}(-1, 1)$	$\mathcal{U}(-1, 1)$	$\mathcal{U}(-1, 1)$
β_{CHEOPS}[b]	–	$\mathcal{U}(-1, 1)$	–	–
		Limb darkening coefficients		
c_{TESS}	$\mathcal{N}(0.696, 0.040) \times \mathcal{U}(0, 1)$	$\mathcal{N}(0.665, 0.006) \times \mathcal{U}(0, 1)$	$\mathcal{N}(0.668, 0.012) \times \mathcal{U}(0, 1)$	$\mathcal{N}(0.725, 0.070) \times \mathcal{U}(0, 1)$
α_{TESS}	$\mathcal{N}(0.722, 0.280) \times \mathcal{U}(0, \infty)$	$\mathcal{N}(0.780, 0.070) \times \mathcal{U}(0, \infty)$	$\mathcal{N}(0.799, 0.060) \times \mathcal{U}(0, \infty)$	$\mathcal{N}(0.600, 0.340) \times \mathcal{U}(0, \infty)$
c_g	$\mathcal{N}(0.814, 0.040) \times \mathcal{U}(0, 1)$	$\mathcal{N}(0.817, 0.006) \times \mathcal{U}(0, 1)$	$\mathcal{N}(0.816, 0.012 \times \mathcal{U}(0, 1)$	$\mathcal{N}(0.824, 0.070) \times \mathcal{U}(0, 1)$
α_g	$\mathcal{N}(1.061, 0.280) \times \mathcal{U}(0, \infty)$	$\mathcal{N}(1.084, 0.070) \times \mathcal{U}(0, \infty)$	$\mathcal{N}(1.119, 0.060) \times \mathcal{U}(0, \infty)$	$\mathcal{N}(0.898, 0.340) \times \mathcal{U}(0, \infty)$
c_r	$\mathcal{N}(0.781, 0.040) \times \mathcal{U}(0, 1)$	$\mathcal{N}(0.751, 0.006) \times \mathcal{U}(0, 1)$	$\mathcal{N}(0.755, 0.012) \times \mathcal{U}(0, 1)$	$\mathcal{N}(0.812, 0.070) \times \mathcal{U}(0, 1)$
α_r	$\mathcal{N}(0.844, 0.280) \times \mathcal{U}(0, \infty)$	$\mathcal{N}(0.869, 0.070) \times \mathcal{U}(0, \infty)$	$\mathcal{N}(0.896, 0.060) \times \mathcal{U}(0, \infty)$	$\mathcal{N}(0.723, 0.340) \times \mathcal{U}(0, \infty)$
c_i	$\mathcal{N}(0.713, 0.040) \times \mathcal{U}(0, 1)$	$\mathcal{N}(0.673, 0.006) \times \mathcal{U}(0, 1)$	$\mathcal{N}(0.677, 0.012) \times \mathcal{U}(0, 1)$	$\mathcal{N}(0.748, 0.070) \times \mathcal{U}(0, 1)$
α_i	$\mathcal{N}(0.721, 0.280) \times \mathcal{U}(0, \infty)$	$\mathcal{N}(0.782, 0.070) \times \mathcal{U}(0, \infty)$	$\mathcal{N}(0.801, 0.060) \times \mathcal{U}(0, \infty)$	$\mathcal{N}(0.600, 0.340) \times \mathcal{U}(0, \infty)$
c_{z_s}	$\mathcal{N}(0.665, 0.040) \times \mathcal{U}(0, 1)$	$\mathcal{N}(0.626, 0.006) \times \mathcal{U}(0, 1)$	$\mathcal{N}(0.630, 0.012) \times \mathcal{U}(0, 1)$	$\mathcal{N}(0.701, 0.070) \times \mathcal{U}(0, 1)$
α_{z_s}	$\mathcal{N}(0.662, 0.280) \times \mathcal{U}(0, \infty)$	$\mathcal{N}(0.728, 0.070) \times \mathcal{U}(0, \infty)$	$\mathcal{N}(0.745, 0.060) \times \mathcal{U}(0, \infty)$	$\mathcal{N}(0.540, 0.340) \times \mathcal{U}(0, \infty)$
c_{CHEOPS}	–	$\mathcal{N}(0.725, 0.006) \times \mathcal{U}(0, 1)$	–	–
α_{CHEOPS}	–	$\mathcal{N}(0.895, 0.070) \times \mathcal{U}(0, \infty)$	–	–
		Baseline		
$\log_{10} \sigma_{\mathrm{GP}}$[c]	$\mathcal{U}(-12, 12)$	$\mathcal{U}(-12, 12)$	$\mathcal{U}(-12, 12)$	$\mathcal{U}(-12, 12)$
$\log_{10} \rho_{\mathrm{GP}}$[c]	$\mathcal{U}(-12, 12)$	$\mathcal{U}(-12, 12)$	$\mathcal{U}(-12, 12)$	$\mathcal{U}(-12, 12)$
$\log_{10} \sigma_{\mathrm{Jit}}$[c]	$\mathcal{U}(-12, 12)$	$\mathcal{U}(-12, 12)$	$\mathcal{U}(-12, 12)$	$\mathcal{U}(-12, 12)$
N[d]	$\mathcal{U}(0, 10)$	$\mathcal{U}(0, 10)$	$\mathcal{U}(0, 10)$	$\mathcal{U}(0, 10)$
X_i[e]	$\mathcal{U}(-10, 10)$	$\mathcal{U}(-10, 10)$	$\mathcal{U}(-10, 10)$	$\mathcal{U}(-10, 10)$

Note. $\mathcal{U}(a, b)$ denotes a uniform prior delimited by a and b; $\mathcal{N}(\mu, \sigma)$ denotes a normal prior with μ mean and σ width.
[a]Centred on ExoFOP tabulated values, with prior σ set to three times the quoted uncertainties.
[b]Negative contamination values are allowed to avoid bouncing effect at the physical boundary of zero contaminants; they could also be caused by systematic offsets.
[c]GP hyperparameters for TESS (shared across sectors).
[d]Normalization factors, i.e. multiplicative factors for the contamination transit models. A factor is fitted for each *TESS* sector and for each ground-based observation.
[e]Coefficients of the linear detrending models for ground-based observation (see Table 1).

Downloaded from academic.oup.com/mnras/article/549/3/stag183/8442244 by UNIV LEIGE FAC PSYCH SCIENCES L'EDUCATION user on 26 November 2026

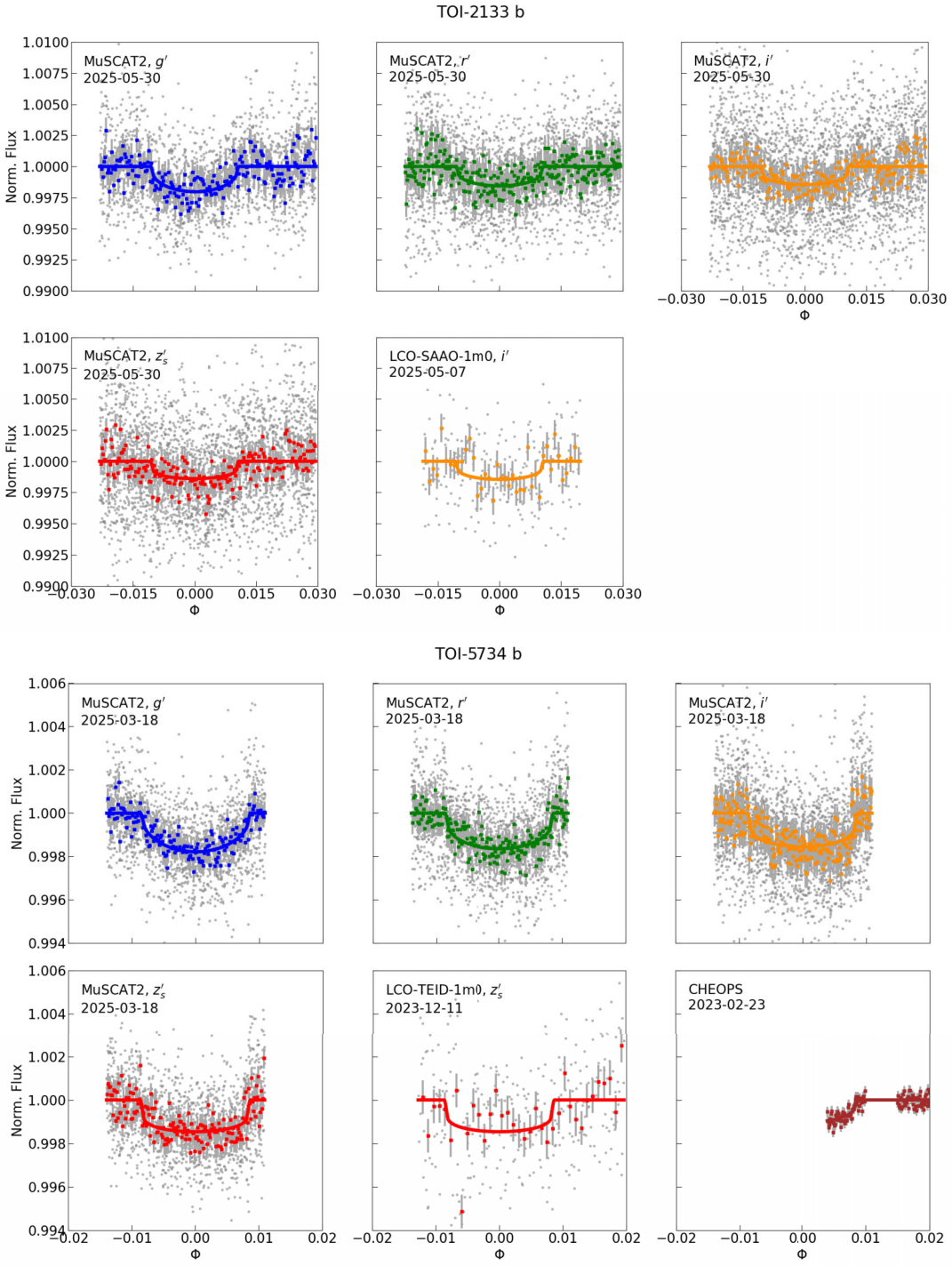


Figure C1. Detrended TFOP light curves for TOI-2133 b and TOI-5734 b, colour-coded according to the passband: g' (blue), r' (green), i' (orange), and z'_s (red).

Downloaded from academic.oup.com/mnras/article/549/3/stag183/8442244 by UNIV LEIGE FAC PSYCH SCIENCES L'EDUCATION user on 26 November 2026

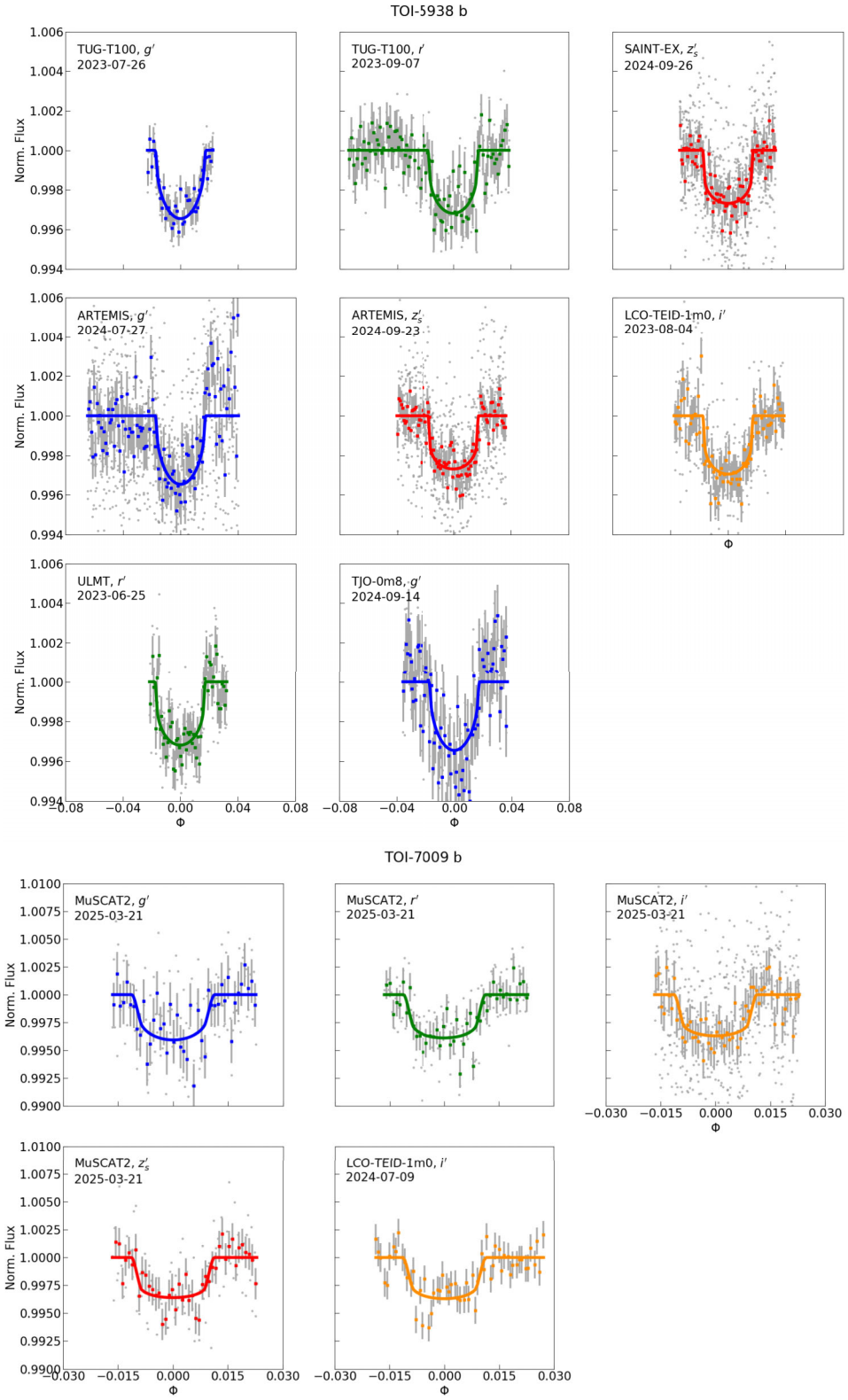


Figure C2. Detrended TFOP light curves for TOI-5938 b and TOI-7009 b, colour-coded as in Fig. C1, plus the CHEOPS passband (brown).

Downloaded from academic.oup.com/mnras/article/549/3/stag183/8442244 by UNIV LEIGE FAC PSYCH SCIENCES L'EDUCATION user on 26 November 2026

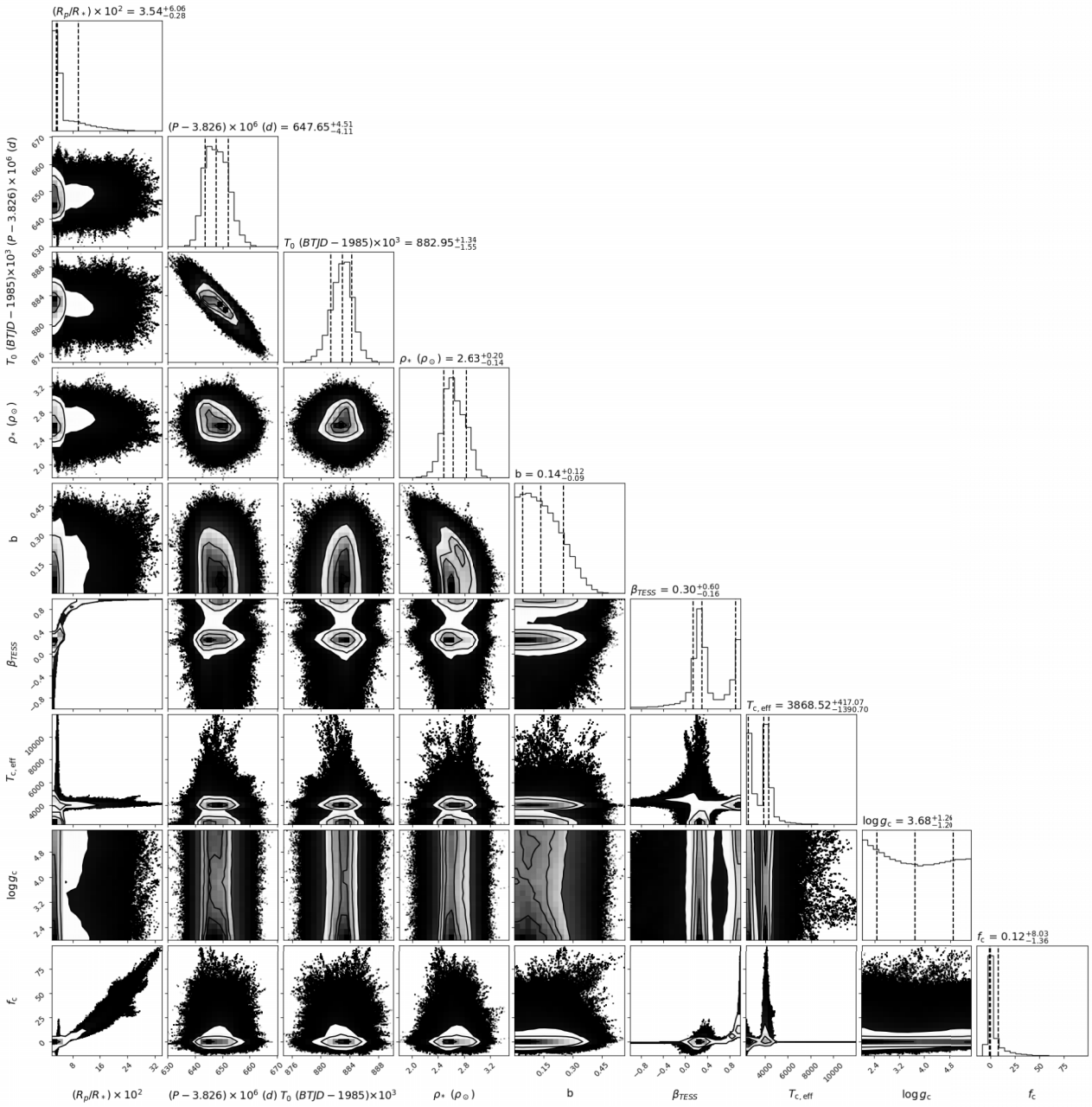


Figure C3. Multicolour photometry cornerplot for TOI-2133 b. The correlation between the contamination parameters (β_{TESS}, $T_{\mathrm{c,eff}}$, and f_c) and the radius ratio ($R_\mathrm{p}/R_\star$) is responsible for the extended tail toward large values of the latter. Such large values are obtained for values of $T_{\mathrm{c,eff}}$ similar to those of the target star, explaining the lack of colour-dependence. This is a well-known limitation of this technique, requiring higher-quality photometric data or complementary information to enable full validation of the planetary candidate.

Downloaded from academic.oup.com/mnras/article/549/3/stag183/8442244 by UNIV LEIGE FAC PSYCH SCIENCES L'EDUCATION user on 26 November 2026

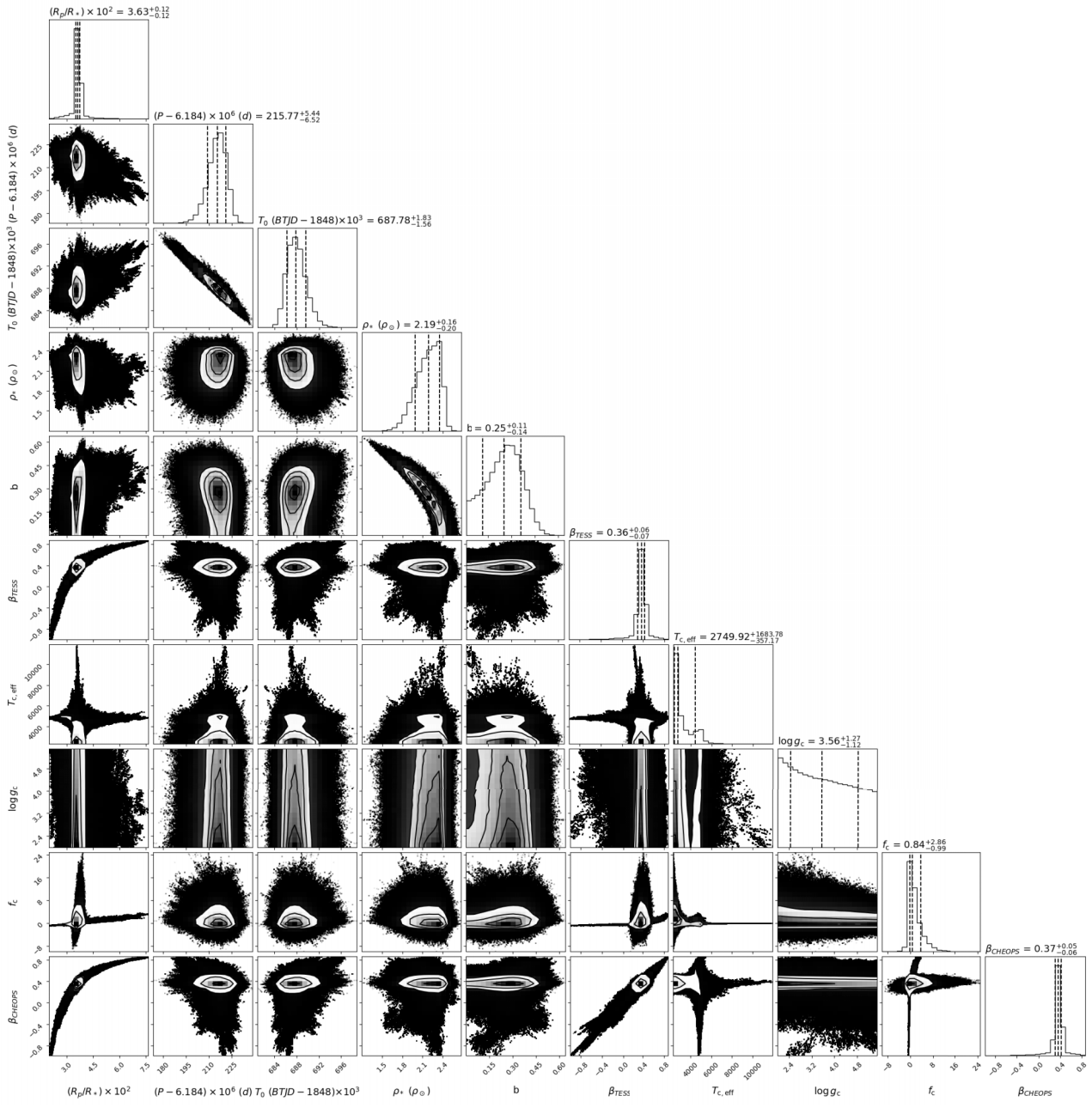


Figure C4. Multicolour photometry cornerplot for TOI-5734 b.

Downloaded from academic.oup.com/mnras/article/549/3/stag183/8442244 by UNIV LEIGE FAC PSYCH SCIENCES L'EDUCATION user on 26 November 2026

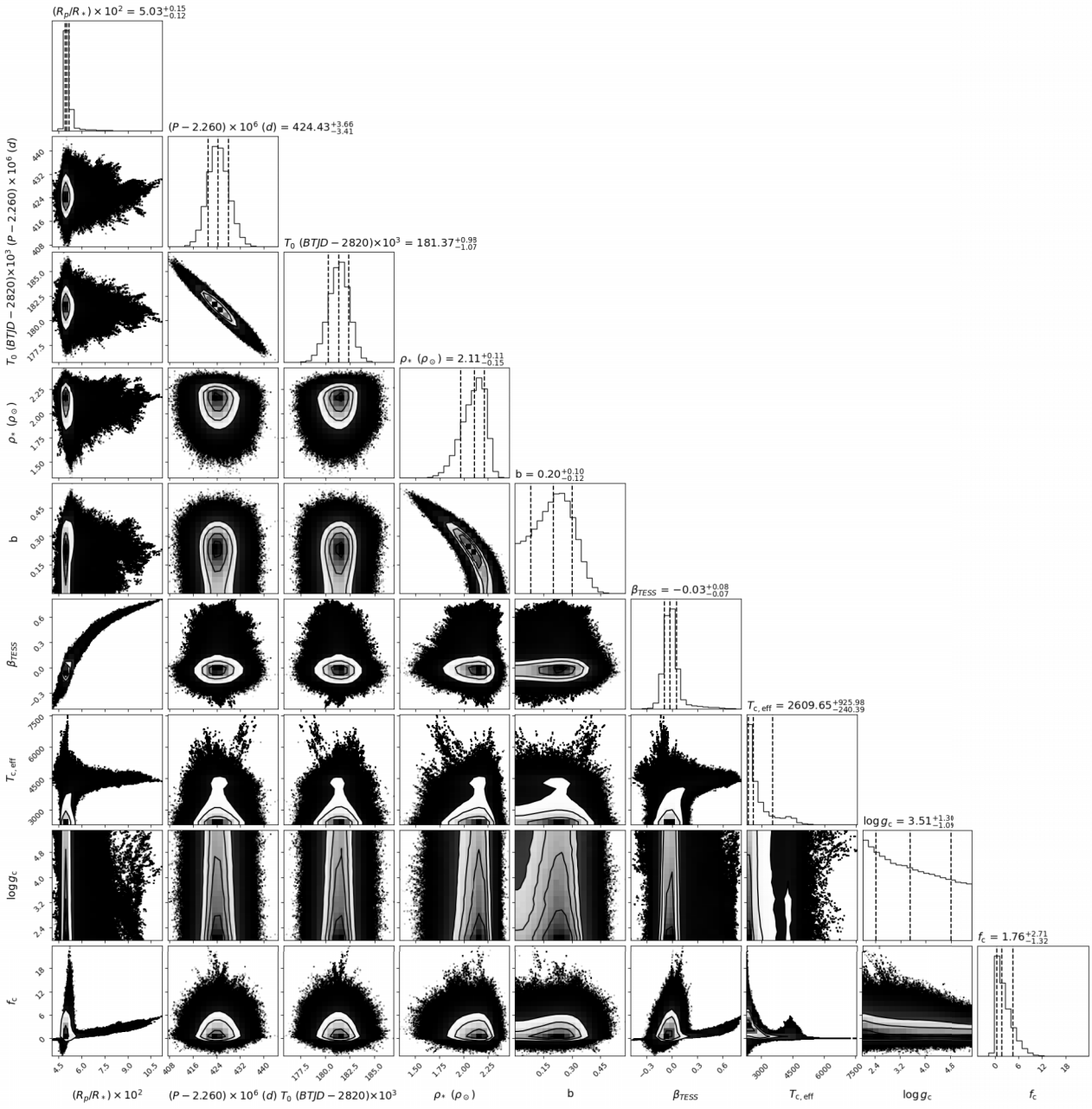


Figure C5. Multicolour photometry cornerplot for TOI-5938 b.

Downloaded from academic.oup.com/mnras/article/549/3/stag183/8442244 by UNIV LEIGE FAC PSYCH SCIENCES L'EDUCATION user on 26 November 2026

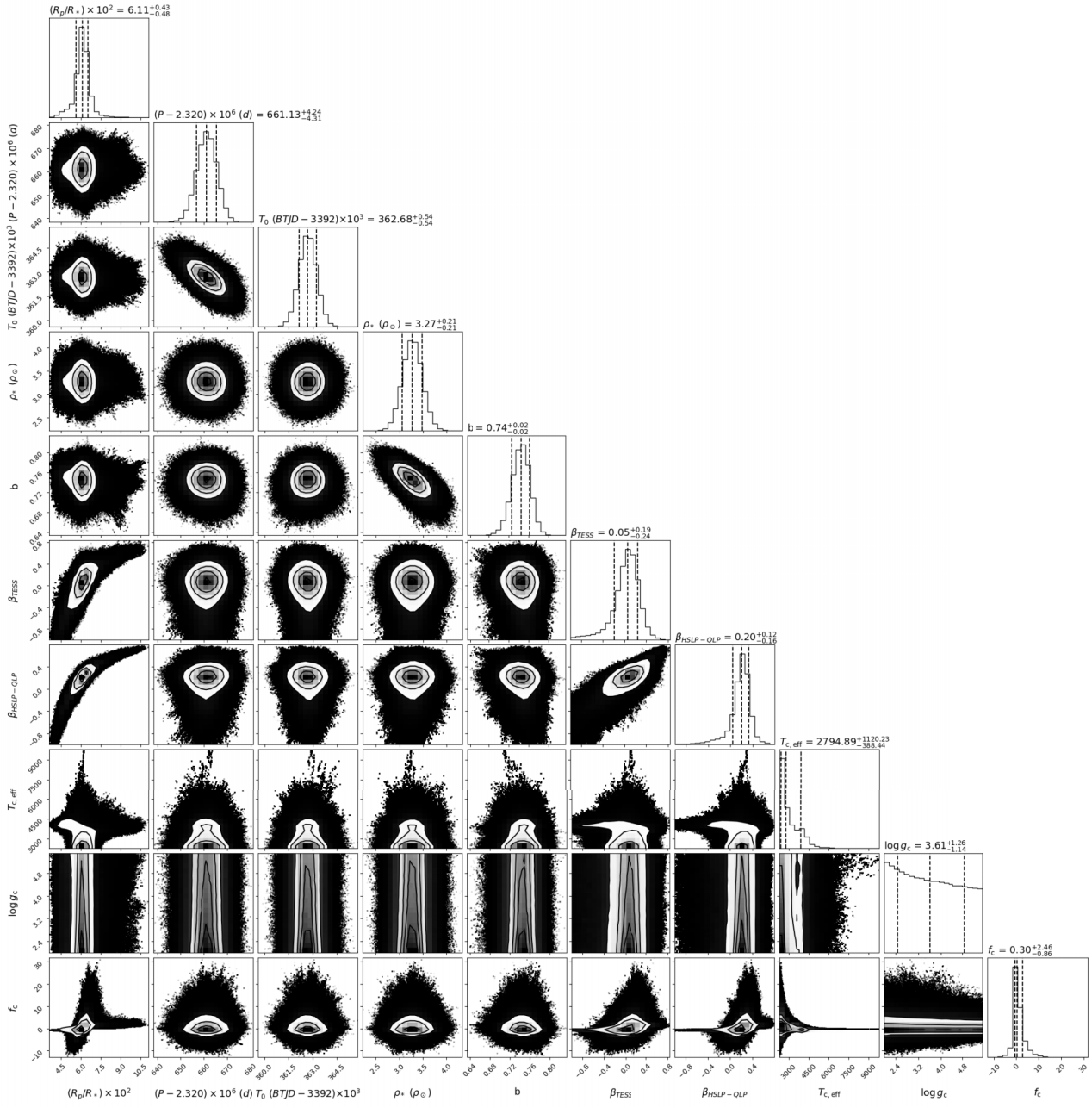


Figure C6. Multicolour photometry cornerplot for TOI-7009 b.

[1]*Instituto de Astrofisica de Andalucía (IAA), Glorieta de la Astronomía s/n, E-18080 Granada, Spain*
[2]*INAF – Palermo Astronomical Observatory, Piazza del Parlamento, 1, I-90134 Palermo, Italy*
[3]*Dpto. Física Teórica y del Cosmos. Universidad de Granada, E-18071 Granada, Spain*
[4]*AI Engineering, Avature, 28004 Madrid, Spain*
[5]*Instituto de Astrofisica de Canarias (IAC), E-38205 La Laguna, Tenerife, Spain*
[6]*Departamento de Astrofisica, Universidad de La Laguna (ULL), E-38206 La Laguna, Tenerife, Spain*
[7]*Komaba Institute for Science, The University of Tokyo, 3-8-1 Komaba, Meguro, Tokyo 153-8902, Japan*
[8]*Instituto de Alta Investigación, Universidad de Tarapacá, Casilla 7D, Arica, Chile*
[9]*Center for Astrophysics | Harvard & Smithsonian, 60 Garden Street, Cambridge, MA 02138, USA*
[10]*Astrobiology Research Unit, Université de Liège, Allée du 6 Août 19C, B-4000 Liège, Belgium*
[11]*Department of Earth, Atmospheric and Planetary Sciences, Massachusetts Institute of Technology, 77 Massachusetts Avenue, Cambridge, MA 02139, USA*
[12]*Department of Astronomy & Space Sciences, Faculty of Science, Ankara University, TR-06100 Ankara, Türkiye*
[13]*Astronomy and Space Sciences Research and Application Center (Kreiken Observatory), Ankara University, Incek Blvd., TR-06837 Ahlatlibel, Ankara, Türkiye*
[14]*Kavli Institute for Astrophysics and Space Research, Massachusetts Institute of Technology, Cambridge, MA 02139, USA*

Downloaded from academic.oup.com/mnras/article/549/3/stag183/8442244 by UNIV LEIGE FAC PSYCH SCIENCES L'EDUCATION user on 26 November 2026

[15]*Department of Astronomy & Astrophysics, University of California San Diego, La Jolla, CA 92093, USA*
[16]*Astrobiology Center, 2-21-1 Osawa, Mitaka, Tokyo 181-8588, Japan*
[17]*Departament d'Astronomia i Astrofísica, Universitat de Valencia, Burjassot E-46100, Spain*
[18]*Department of Multi-Disciplinary Sciences, Graduate School of Arts and Sciences, The University of Tokyo, 3-8-1 Komaba, Meguro, Tokyo 153-8902, Japan*
[19]*Graduate School of Social Data Science, Hitotsubashi University, 2-1 Naka, Kunitachi, Tokyo 186-8601, Japan*
[20]*Okayama Observatory, Kyoto University, 3037-5 Honjo, Kamogatacho, Asakuchi, Okayama 719-0232, Japan*
[21]*Department of Physical Sciences, Ritsumeikan University, Kusatsu, Shiga 525-8577, Japan*
[22]*Freie Universität Berlin, Department of Earth Sciences, Institute of Geological Sciences, Planetary Sciences and Remote Sensing, Malteserstr, 74-100, D-12249 Berlin, Germany*
[23]*Observatoire Astronomique de l'Université de Genève, Chemin Pegasi 51, CH-1290 Versoix, Switzerland*
[24]*Sabadell Astronomical Society, E-08206 Sabadell, Barcelona, Spain*
[25]*National Astronomical Observatory of Japan, 2-21-1 Osawa, Mitaka, Tokyo 181-8588, Japan*
[26]*Astronomical Science Program, Graduate University for Advanced Studies, SOKENDAI, 2-21-1, Osawa, Mitaka, Tokyo 181-8588, Japan*
[27]*Department of Astronomy, University of Texas at Austin, 2515 Speedway, Austin, TX 78712, USA*
[28]*Hazelwood Observatory, 3842 Churchill, Australia*
[29]*Department of Physics and Astronomy, Union College, 807 Union St., Schenectady, NY 12308, USA*
[30]*Società Astronomica Lunae, Castelnuovo Magra, 19037 La Spezia, Italy*
[31]*NSF NOIRLab, 950 N. Cherry Ave., Tucson, AZ 85719, USA*
[32]*NASA Exoplanet Science Institute-Caltech/IPAC, Pasadena, CA 91125, USA*
[33]*School of Physics & Astronomy, University of Birmingham, Edgbaston, Birmingham B15 2TT, UK*
[34]*AIM, CEA, CNRS, Université Paris-Saclay, Université de Paris, F-91191 Gif-sur-Yvette, France*
[35]*Cavendish Laboratory, JJ Thomson Avenue, Cambridge CB3 0HE, UK*
[36]*Institute for Particle Physics and Astrophysics, ETH Zürich, Wolfgang-Pauli-Strasse 2, CH-8093 Zürich, Switzerland*
[37]*Observatory de Ca l'Ou, Sant Martí Sesgueioles, GEECAT, 08282 Barcelona, Spain*
[38]*Institut d'Estudis Espacials de Catalunya (IEEC), C/ Esteve Terrades 1, Edifici RDIT, E-08860 Castelldefels, Spain*
[39]*Observatory Sant Pere, Mataró, GEECAT, 08301 Barcelona, Spain*
[40]*Center for Space and Habitability, University of Bern, Gesellschaftsstrasse 6, CH-3012 Bern, Switzerland*
[41]*Universidad Nacional Autónoma de México, Instituto de Astronomía, AP 70-264, Ciudad de México 04510, México*
[42]*Observatoire de l'Université de Genéve, Chemin des Maillettes 51, CH-1290 Versoix, Switzerland*
[43]*Universidad Nacional Autónoma de México, Instituto de Astronomía, AP 106, Ensenada 22800, BC, México*
[44]*Department of Physics and Astronomy, University of Louisville, Louisville, KY 40292, USA*
[45]*ETH Zurich, Department of Physics, Wolfgang-Pauli-Strasse 2, CH-8093 Zurich, Switzerland*
[46]*Space Research Institute, Austrian Academy of Sciences, Schmiedlstrasse 6, A-8042 Graz, Austria*
[47]*Space Research and Planetary Sciences, Physics Institute, University of Bern, Gesellschaftsstrasse 6, CH-3012 Bern, Switzerland*
[48]*Department of Physics, University of Warwick, Gibbet Hill Road, Coventry CV4 7AL, UK*
[49]*Astrophysics Group, Lennard Jones Building, Keele University, Staffordshire ST5 5BG, UK*
[50]*European Space Agency (ESA), European Space Research and Technology Centre (ESTEC), Keplerlaan 1, NL-2201 AZ Noordwijk, the Netherlands*

This paper has been typeset from a TEX/LATEX file prepared by the author.

Downloaded from academic.oup.com/mnras/article/549/3/stag183/8442244 by UNIV LEIGE FAC PSYCH SCIENCES L'EDUCATION user on 26 November 2026

© The Author(s) 2026.
Published by Oxford University Press on behalf of Royal Astronomical Society. This is an Open Access article distributed under the terms of the Creative Commons Attribution License (https://creativecommons.org/licenses/by/4.0/), which permits unrestricted reuse, distribution, and reproduction in any medium, provided the original work is properly cited.